

## A Finite Volume Method for the Multi Subband Boltzmann Equation with Realistic 2D Scattering in Double Gate MOSFETs

Tiao Lu<sup>1</sup>, Gang Du<sup>2</sup>, Xiaoyan Liu<sup>2</sup> and Pingwen Zhang<sup>1,\*</sup>

<sup>1</sup> School of Mathematical Sciences, LMAM and CAPT, Peking University, Beijing 100871, China.

<sup>2</sup> Institute of Microelectronics, Peking University, Beijing 100871, China.

Received 7 November 2009; Accepted (in revised version) 26 November 2010

Available online 27 April 2011

---

**Abstract.** We propose a deterministic solver for the time-dependent multi-subband Boltzmann transport equation (MSBTE) for the two dimensional (2D) electron gas in double gate metal oxide semiconductor field effect transistors (MOSFETs) with flared out source/drain contacts. A realistic model with six-valleys of the conduction band of silicon and both intra-valley and inter-valley phonon-electron scattering is solved. We propose a second order finite volume method based on the positive and flux conservative (PFC) method to discretize the Boltzmann transport equations (BTEs). The transport part of the BTEs is split into two problems. One is a 1D transport problem in the position space, and the other is a 2D transport problem in the wavevector space. In order to reduce the splitting error, the 2D transport problem in the wavevector space is solved directly by using the PFC method instead of splitting into two 1D problems. The solver is applied to a nanoscale double gate MOSFET and the current-voltage characteristic is investigated. Comparison of the numerical results with ballistic solutions show that the scattering influence is not ignorable even when the size of a nanoscale semiconductor device goes to the scale of the electron mean free path.

**AMS subject classifications:** 35Q20, 35Q40, 65Z05

**Key words:** Double gate MOSFET, multi subband Boltzmann transport equation, 2D electron gas, deterministic solver, PFC method.

---

## 1 Introduction

The down-scaling is an important engine in the semiconductor industry. With the size of the semiconductor enters the deep sub-micro range, the conventional bulk MOSFET

---

\*Corresponding author. *Email addresses:* tlu@math.pku.edu.cn (T. Lu), gangdu@pku.edu.cn (G. Du), xyliu@ime.pku.edu.cn (X. Liu), pzhang@math.pku.edu.cn (P. Zhang)

faces great challenge to be scaled down to 40 nm because of the short channel effects (SCEs) [3]. The SCEs modify the threshold voltage and the electron drift characteristics in the channel, so cause considerable distress for the device designers. The double gate (DG) MOSFET is a promising structure for next generation semiconductors because it provides an extra gate to suppress the SCEs. So its simulation has drawn the interest of many researchers, e.g., [1, 6, 15, 19].

The double gate MOSFETs with a channel length greater than the mean free path of electrons can still use the semi-classical transport equation in the transport direction. But when the thickness of the Si body between the two gate stacks becomes thin, the quantum confinement results in energy quantization. The quantization's influence to the electron transport can not be disregarded. The quantum models like the nonequilibrium Green function (NEGF) method [7], the density matrix method and the Wigner transport equation are not mature enough for the devices with a channel length greater than the mean free path of electrons. These quantum-mechanical methods can be applied to the RTD and quantum dots, wires and wells and molecular devices where the electron scattering can be neglected [24]. The model under consideration in this paper solves the multi sub-band Boltzmann transport equation (BTE) self-consistently with the Schrödinger equation and the Poisson equation. So we can call it the Boltzmann-Schrödinger-Poisson (BSP) system.

Many deterministic solvers for the BTE have been proposed to solve the Boltzmann-Poisson system, such as the WENO solver [5], the spherical harmonic expansion (SHE) method [25], the deterministic particle method [8], the finite-difference scheme [10, 18]. The positive and flux conservative (PFC) method using a splitting approach (which splits a multi-dimensional problem into many 1D problems) has been proposed in [12] to solve the transport part of the BTE (the Vlasov equation). The PFC method is not only conservative, but also preserves the positivity and the maximum value of the distribution function. Recently, Ben Abdallah et al. present a deterministic solver of the Boltzmann-Schrödinger-Poisson system with an effective valley and a very simple scattering term (relaxation time approximation) [1]. The quantum confinement in the  $z$ -direction forms 2D electron gas (2DEG), so the scattering should be considered as  $2Dk$  scattering. However, the deterministic methods for the Boltzmann-Schrödinger-Poisson system with  $2Dk$  scattering has not been well investigated.

The relaxation time approximation is questionable when the size of the devices is comparable with the mean free path of electrons and the system is far away from the equilibrium (the high source-drain voltage  $V_{DS}$  often drives the system far away from the equilibrium). High doping density requires the consideration of the Pauli exclusion principle. In this paper, we present a deterministic solver for a more complete time-dependent Boltzmann-Schrödinger-Poisson system. Here "more complete" means in two aspects: (1) the six valleys of  $\Delta$ -band instead of an effective valley of silicon are considered; and (2) the intra-valley and inter-valley phonon-electron  $2Dk$  scattering including the Pauli exclusion principle is considered, instead of only a relaxation time approximation of scattering. We include an acoustic phonon and an optical phonon for the intra-

valley scattering and both  $f$ -type and  $g$ -type scattering for the inter-valley scattering.

For the scattering part, we use the coordinate transformation  $(k_x, k_y) \rightarrow (\omega, \theta)$ , and the property of  $\delta$ -function in the scattering operator to integrate the scattering integral with respect to the energy  $\omega$  exactly. Then, by integrating over a control volume, we obtain a numerical scheme for discretization of the scattering integral which preserves the property that the scattering mechanism only transfers an electron from one state to another state and does not change the number of electrons in a space mesh.

We use a second order time splitting method [23] to split the time-dependent BTE into the transport part and the scattering part. Since we have adopted the coordinate transformation  $(k_x, k_y) \rightarrow (\omega, \theta)$  to simplify the integration of the scattering part, the transport part of the BTE is three dimensional uncoupled problem  $(x, \omega, \theta)$  instead of being a two dimensional problem  $(x, k_x)$  where  $k_y$  can be treated as a parameter. We use the PFC method to solve the transport part. In order to make use the fact that the force is only nonzero in the  $x$ -direction and to reduce the splitting error, we split the transport part into two problems (a 1D problem for  $x$ -advection and a 2D problem for  $\omega$ -/ $\theta$ - advection) instead of split it into three 1D problems ( $x$ -advection,  $\omega$ -advection,  $\theta$ -advection).

The initial values (subbands, eigen wavefunctions, etc) are obtained by solving one of two self-consistent Schrödinger-Poisson systems described in Subsection 2.3. Due to high doping density, the distribution functions at the source and drain contacts are assume to be the Fermi-Dirac distributions instead of the Boltzmann distributions. In order to obtain a current-voltage curve, the device under a series of source-drain bias voltages from low to high needs to be simulated. The potential and distribution functions obtained at a low voltage are used as the initial values of the next higher voltage. A standard centered finite difference method is used to discretize the Poisson equation and Schrödinger equations. The deterministic solver is parallelized with the help of Trilinos [16] to reduce the computation time.

The paper is organized as follows. In Section 2, we describe the time-dependent Boltzmann-Schrödinger-Poisson system. In Section 3, the numerical scheme is described, with emphasis on the finite volume method based on the PFC method for the ballistic part of the BTE. In Section 4, numerical results of simulating an ultra thin DG MOSFET are given. A conclusion is provided in the final section.

## 2 Time-dependent multi-subband BTE model

A double gate (DG) MOSFET with flared out source/drain contacts is illustrated in Fig. 1, where the real flared out source/drain contacts are not plotted.  $AB/FG$  in Fig. 1 are the ends of the heavily doped region that are connected to the flared out source/drain (S/D) contacts. We will treat  $AB$  and  $FG$  as the "ideal" S/D contacts and apply some appropriate boundary conditions at  $AB/FG$  as in [20]. The silicon layer is doped with a heavy doping density  $N_D = N_{SD}$  or a light doping density  $N_D = N_b$ . The two heavily doped regions have the same length  $L_{SD}$  and we call them the S/D extensions. The

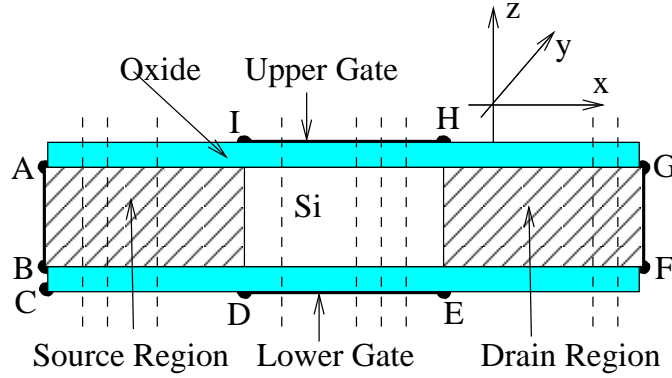


Figure 1: Schematic of the thin body DG MOSFET structure. The device is assumed to be infinitely wide in the  $y$ -direction, and the potential is assumed to be translationally invariant along the width. The silicon layer is stacked by two oxide layers. The two squares blend oblique lines denote the heavily doped regions (they are called S/D extensions).  $AB/FG$  are connected to the real source/drain contacts through a flared out region (a contact with a flared out region is called a flared out contact).  $DE/HI$  are connected to the lower/upper gate electrodes. Elsewhere are the Oxide/Air interfaces.

lightly doped region between two heavy doped regions is called the channel region and its length is  $L_{Ch}$ . In the channel region, a potential barrier will be formed.  $DE/IH$  in Fig. 1 are connected to the lower/upper gate contacts which are used to modulate the height and shape of the barrier and further to adjust the current from source to drain  $I_{DS}$ . The total distance between the "ideal" S/D contacts  $L = 2L_{SD} + L_{Ch}$  is the length of the part of the device we simulate. The thickness of the silicon layer is denoted by  $T_{Si}$ . In this paper, we set  $T_{Si} = 3\text{nm}$ . For such a thin silicon channel, the quantum effect resulted from the quantum size confinement plays an important role in studying the characteristics of a device. The thickness of each oxide layer is  $T_{Ox}$ .

We introduce the multi-subband BTE (MSBTE) in this section shortly here. One can refer to [1, 20, 24] for more information of MSBTE. MSBTE consists of a set of coupled BTEs describing transport in the subbands

$$\frac{\partial f_i}{\partial t} + v_i \frac{\partial f_i}{\partial x} + \frac{F_i}{\hbar} \frac{\partial f_i}{\partial k_x} = \frac{\partial f_i}{\partial t} \Big|_{\text{Scat}}, \quad x \in (0, L), \quad (2.1)$$

where  $f_i(t, x, \mathbf{k})$  is the probability distribution function of the wavevector  $\mathbf{k}$  at the position  $x$  in the subband  $i$ . Coupling occurs due to inter-subband scattering. The electron transport is along the  $x$  direction. We choose the left bottom point C in Fig. 1 as the original point of the  $xOz$  plane. The wave vector  $\mathbf{k} = (k_x, k_y)$ . The subband index  $i$  can be split into a valley index  $\nu$  and an index  $j$ , which is the index of the eigenvalues of the effective mass Schrödinger equation for the  $\nu$ 'th valley. We choose the six ellipsoidal parabolic  $\Delta$  valleys.  $v_i$  is the velocity of electrons in the subband  $i$

$$v_i = \frac{1}{\hbar} \frac{\partial \mathcal{E}_i}{\partial k_x}, \quad (2.2)$$

and  $F_i$  is the force in the  $x$  direction and is equal to

$$F_i = -\frac{\partial \mathcal{E}_i}{\partial x}, \quad (2.3)$$

where  $\mathcal{E}_i$  is the total energy of the electron at  $(x, \mathbf{k})$  in the subband  $i$  (see Eqs. (2.6) and (2.7)).

The electrons in the real S/D contacts (electron reservoirs) are in equilibrium characterized by a Fermi level  $E_{F1}/E_{F2}$ . The source Fermi level  $E_{F1}$  will be set to be 0 in this paper. The Fermi level offset between the source and drain contacts is equal to the applied S/D bias voltage  $V_{DS}$  times  $-q_e$ , i.e.,  $E_{F2} - E_{F1} = -q_e V_{DS}$ , where  $q_e$  denotes the positive electron charge.  $AB/FG$  in Fig. 1 are contacted to the S/D contacts through a flared out region. The potential at the  $AB/FG$  may not equal to the potential at the real source contact, but the electrons at the  $AB/FG$  injected from the real flared out contacts are assumed to have the same the Fermi level as that in the real contacts which are external to the region being simulated [20]. That is why we use  $E_{F1}$  and  $E_{F2}$  in Eq. (2.4) to express the probability distribution density of the injected electrons. The potential at the  $AB/FG$  is allowed to float to some value in order to fulfill the charge neutrality at the  $AB/FG$ . More about this will be explained when we discuss the boundary conditions for the Poisson equation. Therefore we set the inflow distribution function at  $AB/FG$  to be

$$f_i(t, 0, \mathbf{k}) = \left[ 1 + \exp\left(\frac{\mathcal{E}_i(0) - E_{F1}}{k_B T}\right) \right]^{-1}, \quad \text{if } k_x > 0, \quad (2.4a)$$

$$f_i(t, L, \mathbf{k}) = \left[ 1 + \exp\left(\frac{\mathcal{E}_i(L) - E_{F2}}{k_B T}\right) \right]^{-1}, \quad \text{if } k_x < 0, \quad (2.4b)$$

where  $k_B$  is the Boltzmann constant, and  $T$  is the lattice temperature. We use  $V_t = k_B T / q_e$  to denote the thermal voltage. In this paper,  $T = 300$  K and the values of  $V_t$  at  $T = 300$  K are given in Table 1. The initial distribution  $f_i(0, x, \mathbf{k})$  will be given by solving a Schrödinger-Poisson system described in Subsection 2.3.

The device cross-section is partitioned into  $N_x$  sections along the channel direction  $x$ . At each section, the Schrödinger equation

$$\left[ -\frac{\hbar^2}{2m_{z,v}} \frac{\partial^2}{\partial z^2} - q_e V(t, x, z) \right] \varphi_{v,j,x}(z) = E_{v,j,x}(t) \varphi_{v,j,x}(t, z), \quad z \in (T_{Ox}, T_{Ox} + T_{Si}) \quad (2.5)$$

is solved in the  $z$  direction (the confinement direction). Here  $x$  is the position of one of the slices illustrated in Fig. 1,  $V(t, x, z)$  is the electrostatic potential and  $m_{z,v}$  is the effective mass in the  $z$ -direction for the electrons in the  $v$ 'th valley.  $m_{z,v}$  is either equal to the transverse effective mass  $m_t = 0.19m_0$  or the longitudinal effective mass  $m_l = 0.916m_0$ , where  $m_0$  is the free electron rest mass. The wavefunction at the Si/Oxide interface is assumed to be zero, i.e., the boundary condition is  $\varphi(T_{Ox}) = \varphi(T_{Ox} + T_{Si}) = 0$ . The eigen energy  $E_{v,j,x}(t)$  and the eigen wavefunction  $\varphi_{v,j,x}(t, z)$  are obtained at each position  $x$ . The  $t$  variable in  $V(t, x, z)$ ,  $E_{v,j,x}(t)$  and  $\varphi_{v,j,x}(t, z)$  will be omitted for brevity. We then regard

$E_{v,j,x}$  as a function of  $x$  and write it into  $E_{v,j}(x)$ . It is easily seen that  $E_{v,j}(x)$  consists of two parts. One is from the quantum confinement in the  $z$  direction, and the other is from the electrostatic potential energy  $-q_e V(x,z)$ . The total energy of the electron at  $(x, \mathbf{k})$  in the subband  $(v, j)$  is

$$\mathcal{E}_{v,j}(t, x, \mathbf{k}) = E_{v,j}(t, x) + \omega_v(\mathbf{k}), \quad (2.6)$$

where  $\omega_v(\mathbf{k})$  is the dispersion relation. In this paper, we approximate the dispersion relation with the parabolic approximation

$$\omega_v(\mathbf{k}) = \frac{\hbar^2 k_x^2}{2m_{x,v}} + \frac{\hbar^2 k_y^2}{2m_{y,v}}, \quad (2.7)$$

where  $m_{x,v}/m_{y,v}$  are the effective mass in the  $x/y$  direction of the  $v$ 'th valley.

To include the change of the potential due to the redistribution of electrons, we solve the Poisson equation

$$-\nabla_{x,z} \cdot (\epsilon(x,z) \nabla_{x,z} V(x,z)) = Q, \quad (x,z) \in (0,L) \times (0,L_z), \quad (2.8)$$

in both the silicon layer and two oxide layers, where  $L_z = 2T_{Ox} + T_{Si}$  is the total thickness of the device,  $V(x,z)$  is the electrostatic potential, and  $\epsilon(x,z)$  is the permittivity of the material and  $\epsilon(x,z) = \epsilon_{Si} = 3.9\epsilon_0$  in the silicon layer, and  $\epsilon(x,z) = \epsilon_{SiO_2} = 11.7\epsilon_0$  in the oxide layer.  $Q$  is the charge density

$$Q = \begin{cases} q_e(N_D(x) - n(x,z)), & \text{if } z \in (T_{Ox}, T_{Ox} + T_{Si}), \\ 0, & \text{else,} \end{cases} \quad (2.9)$$

where the doping density is only nonzero in the silicon layer and is either equal to the heavy doping density  $N_{SD}$  in the S/D extensions or  $N_b$  in the channel region. The electron density  $n(x,z)$  in the silicon layer is calculated by

$$n(x,z) = \frac{1}{2\pi^2} \sum_i \iint_{\mathbb{R}^2} f_i dk_x dk_y |\varphi_{i,x}(z)|^2, \quad (2.10)$$

which means the electron density at each slice  $x$  in the subband  $i$  is proportional to the square modulus of the corresponding eigen wavefunction in the  $z$ -direction. The electrostatic potential  $V$ , the charge density  $Q$  and the electron density  $n$  are all time-dependent, while we have omitted  $t$  variable for brevity.

For the Poisson equation, the boundary conditions at the gate electrodes (Dirichlet) and at the Oxide/Air interfaces (Neumann) are standard. At the Oxide/Gate interface  $DE/HI$  in Fig. 1, the potential is equal to the upper/lower gate voltage  $V_{G_u,S}/V_{G_d,S}$ . At the Oxide/Air interfaces, the natural boundary condition  $\partial V(x,z)/\partial n = 0$  is applied, where  $\mathbf{n}$  is the unit outward norm of the boundary. Boundary conditions at the interface between the S/D extensions and the flared out contacts are dealt with a simple effective method proposed in [20]. Instead of including the flared out region to explore the resistive drops

that may occur at the wide/narrow transition, the authors of [20] use the natural boundary condition at  $AB/FG$  in Fig. 1. In [20], an argument is given why such a boundary condition works. One important assumption in [20] is that the Fermi levels at the flared out S/D contacts are fixed because the S/D contacts are electron reservoirs and the electrons flying in/out of the device do not influence the electron distribution in the S/D contacts. When the source-drain voltage  $V_{DS}$  is large, the electrons at the S/D extensions is far from the equilibrium. We take the source extension as an example to explain this point. The distribution function at  $k_x < 0$  is much less than the distribution at  $k_x > 0$  due to few electrons are reflected by the build-in barrier lowered by the high  $V_{DS}$ . But at  $AB$  in Fig. 1, the electrons with  $k_x > 0$  are injected from the real flared out source contact, and have the same Fermi level as the source contact (see (2.4)). So the neutrality at the  $AB$  can not be fulfilled if a fixed potential is used here. Therefore the authors of [20] use a floating boundary condition to allow the potential to float to an appropriate value to fulfill the neutrality and thus define their "ideal" contacts. Scattering occurs much fewer in nanoscale devices (excluding the flared out contacts) than in the traditional scattering-dominated long channel devices, so the scattering can not scatter enough electrons to  $k_x < 0$  in the source extensions. Therefore the floating boundary conditions are also used even when the scattering exists.

Up till now we have introduced a set of BTEs in many subbands, and Schrödinger equations at all slices, and a two dimensional Poisson equations. Next, we will introduce the scattering term  $(\partial f_i / \partial t)|_{\text{Scat}}$  including the intra-valley scattering and the inter-valley scattering of the 2DEG [2].

## 2.1 Scattering of the 2DEG

Lattice vibrations are an inevitable source of scattering and can dominate the scattering near room temperature. We consider three types of scattering by lattice vibrations, i.e., the intra-valley acoustic phonon-electron (AP) scattering, the intra-valley optical phonon-electron (OP) scattering and the inter-valley optical phonon-electron (IOP) scattering.

The right hand side of the BTE (2.1) can be written into the sum of different scattering terms

$$\frac{\partial f_i}{\partial t} \Big|_{\text{Scat}} = \sum_{\chi} \frac{\partial f_i}{\partial t} \Big|_{\chi}, \quad (2.11)$$

where the index  $\chi$  is used to denote different kinds of scattering. One kind of scattering  $(\partial f_i / \partial t)|_{\chi}$  in (2.11) can be written into

$$\begin{aligned} \frac{\partial f_i}{\partial t} \Big|_{\chi} = & \sum_{i'} \frac{1}{(2\pi)^2} \iint_{\mathbb{R}^2} S_{\chi}^{\text{Absp}}(\mathbf{k}', i'; \mathbf{k}, i) f_{i'}(t, x, \mathbf{k}') (1 - f_i(t, x, \mathbf{k})) d^2 \mathbf{k}' \\ & - \sum_{i'} \frac{1}{(2\pi)^2} \iint_{\mathbb{R}^2} S_{\chi}^{\text{Emss}}(\mathbf{k}, i; \mathbf{k}', i') f_i(t, x, \mathbf{k}) (1 - f_{i'}(t, x, \mathbf{k}')) d^2 \mathbf{k}', \end{aligned} \quad (2.12)$$

where  $S_{\chi}^{\text{Absp}}(\mathbf{k}', i'; \mathbf{k}, i)$  is the scattering rate of the electron transition from the state  $(\mathbf{k}', i')$  to the state  $(\mathbf{k}, i)$  (in short  $(\mathbf{k}', i') \rightarrow (\mathbf{k}, i)$ ) due to the absorption of a phonon with an energy  $E_{\chi}$ , and  $S_{\chi}^{\text{Emss}}(\mathbf{k}, i; \mathbf{k}', i')$  is the scattering rate of the electron transition  $(\mathbf{k}, i) \rightarrow (\mathbf{k}', i')$  due to the emission of a phonon with an energy  $E_{\chi}$ . In short, we can express the meaning of  $S_{\chi}^{\text{Absp}}(\mathbf{k}', i'; \mathbf{k}, i)$  by

$$S_{\chi}^{\text{Absp}}(\mathbf{k}', i'; \mathbf{k}, i) = \text{rate of } (\mathbf{k}', i') \xrightarrow{\text{Absorption } E_{\chi}} (\mathbf{k}, i),$$

and  $S_{\chi}^{\text{Emss}}(\mathbf{k}, i; \mathbf{k}', i')$  by

$$S_{\chi}^{\text{Emss}}(\mathbf{k}, i; \mathbf{k}', i') = \text{rate of } (\mathbf{k}', i') \xrightarrow{\text{Emission } E_{\chi}} (\mathbf{k}, i).$$

Note that  $S_{\chi}^{\text{Absp}}(\mathbf{k}', i'; \mathbf{k}, i)$  and  $S_{\chi}^{\text{Emss}}(\mathbf{k}, i; \mathbf{k}', i')$  are only nonzero when  $\mathcal{E}_{i'}(x, \mathbf{k}') + E_{\chi} = \mathcal{E}_i(x, \mathbf{k})$  due to the requirement of the energy conservation (see (2.14a)). The  $S_{\chi}^{\text{Absp}}$  part of (2.12) denotes the electrons at the state  $(\mathbf{k}, i)$  are increased due to the electrons at the state  $(\mathbf{k}', i')$  absorbing a phonon ( $E_{\chi}$ ). We allow  $E_{\chi} < 0$  to include the case that the electrons at the state  $(\mathbf{k}, i)$  are increased due to the electrons at the state  $(\mathbf{k}', i')$  emitting a phonon. The same way is done to the  $S_{\chi}^{\text{Emss}}$  part of (2.12). We take an example to explain this. For example, there are two kinds of scattering with  $\chi = 1$  and  $\chi = 2$  in (2.11) corresponding to the OP scattering with a phonon energy  $\hbar\omega_{op}$  (given in Table 1). First, we set  $E_{\chi=1} = \hbar\omega_{op}$ , for the first kind of scattering, so we have

$$S_{\chi=1}^{\text{Absp}}(\mathbf{k}', i'; \mathbf{k}, i) = \text{rate of } (\mathbf{k}', i') \xrightarrow{\text{Absorption } \hbar\omega_{op}} (\mathbf{k}, i),$$

$$S_{\chi=1}^{\text{Emss}}(\mathbf{k}, i; \mathbf{k}', i') = \text{rate of } (\mathbf{k}, i) \xrightarrow{\text{Emission } \hbar\omega_{op}} (\mathbf{k}', i').$$

Then we set  $E_{\chi=2} = -\hbar\omega_{op}$ , for the second kind of scattering. From the physical meaning of the scattering rate, we can obtain

$$S_{\chi=2}^{\text{Absp}}(\mathbf{k}', i'; \mathbf{k}, i) = S_{\chi=1}^{\text{Emss}}(\mathbf{k}, i; \mathbf{k}', i'), \quad S_{\chi=2}^{\text{Emss}}(\mathbf{k}, i; \mathbf{k}', i') = S_{\chi=1}^{\text{Absp}}(\mathbf{k}', i'; \mathbf{k}, i) \quad (2.13)$$

for the second kind of scattering. The relation (2.13) describes that "absorbing" an imaginary phonon with a negative energy is equivalent to emitting a real phonon with a positive energy. Since we can make use of the relation (2.13) to get the scattering rates for  $E_{\chi} < 0$  using the scattering rates for  $E_{\chi} > 0$ , we only need to give the formulas of the scattering rates for  $E_{\chi} > 0$ .

The OP scattering rates for  $E_{\chi} > 0$  can be expressed into

$$S_{\chi}^{\text{Absp}}(\mathbf{k}', i'; \mathbf{k}, i) = K_{\chi} \delta(\mathcal{E}_{i'}(x, \mathbf{k}') + E_{\chi} - \mathcal{E}_i(x, \mathbf{k})) N_{\chi} I_{ii'}(x), \quad (2.14a)$$

$$S_{\chi}^{\text{Emss}}(\mathbf{k}, i; \mathbf{k}', i') = S_{\chi}^{\text{Absp}}(\mathbf{k}', i'; \mathbf{k}, i) (N_{\chi} + 1) N_{\chi}^{-1}, \quad (2.14b)$$

where

$$K_\chi = \frac{\pi D_\chi^2}{\rho_0 \omega_\chi}, \quad (2.15a)$$

$$I_{ii'}(x) = \int_0^{T_{Si}} |\varphi_{i,x}(z) \varphi_{i',x}(z)|^2 dz, \quad (2.15b)$$

$N_\chi = (e^{E_\chi/k_B T} - 1)^{-1}$  is the occupation number of phonons, and  $D_\chi = D_{op}$  is the deformation potential parameter for the OP scattering whose value used in this paper is given in Table 1.

Table 1: The physical constants and some parameters.

|  |   |  |
|--|---|--|
| $m_0 = 5.69 \times 10^{-16} \text{eVs}^2 \text{cm}^{-2}$ | $q_e = 1.602177 \times 10^{-19} \text{C}$ | $\epsilon_0 = 8.854188 \times 10^{-14} \text{Fcm}^{-1}$      |
| $k_B T = 0.02586 \text{eV}$                              | $V_t = k_B T / q_e = 0.02586 \text{V}$    | $\hbar = 6.582122 \times 10^{-16} \text{eVs}$                |
| $E_{ac} = 9 \text{eV}$                                   | $u_s = 9.04 \times 10^5 \text{cms}^{-1}$  | $\rho_0 = 1.4547 \times 10^{12} \text{eVs}^2 \text{cm}^{-5}$ |
| $D_{op} = 1.556 \times 10^9 \text{eVcm}^{-1}$            | $\hbar \omega_{op} = 0.062 \text{eV}$     | $x_{\text{ref}} = 10^{-7} \text{cm}$                         |

Table 2: Parameters for the inter-valley X-X scattering rate of Silicon [22].

|                          |                                    |                          |                                    |                          |                                    |
|--------------------------|------------------------------------|--------------------------|------------------------------------|--------------------------|------------------------------------|
| $D_{XX}^{s1}$            | $0.5 \times 10^8 \text{eVcm}^{-1}$ | $D_{XX}^{s2}$            | $0.8 \times 10^8 \text{eVcm}^{-1}$ | $D_{XX}^{s3}$            | $1.1 \times 10^9 \text{eVcm}^{-1}$ |
| $\hbar \omega_{XX}^{s1}$ | $0.01206 \text{eV}$                | $\hbar \omega_{XX}^{s2}$ | $0.01853 \text{eV}$                | $\hbar \omega_{XX}^{s3}$ | $0.06204 \text{eV}$                |
| $D_{XX}^{f1}$            | $0.3 \times 10^8 \text{eVcm}^{-1}$ | $D_{XX}^{f2}$            | $2.0 \times 10^8 \text{eVcm}^{-1}$ | $D_{XX}^{f3}$            | $2.0 \times 10^8 \text{eVcm}^{-1}$ |
| $\hbar \omega_{XX}^{f1}$ | $0.01896 \text{eV}$                | $\hbar \omega_{XX}^{f2}$ | $0.04739 \text{eV}$                | $\hbar \omega_{XX}^{f3}$ | $0.05903 \text{eV}$                |

The inter-valley scattering process can be classified into *f*-type and *g*-type processes. A process is referred to as *f*-type, if the initial and final orientations are different, otherwise as *g*-type. The parameters of both *f*-type and *g*-type scattering processes are listed in Table 2. The formulas (2.14a), (2.14b) and (2.15a) are still applicable for the IOP scattering. But the values of  $E_\chi$  and  $D_\chi$  are different. We use six pairs of parameters in Table 2. For example, the inter-valley optical phonon with a pair of parameters  $(\hbar \omega_{XX}^{s1}, D_{XX}^{s1})$  corresponds to two kinds of scattering  $\chi=3$  and  $\chi=4$ . Plugging  $E_{\chi=3} = \hbar \omega_{XX}^{s1}$  and  $D_{\chi=3} = D_{XX}^{s1}$  into (2.14a) and (2.14b) yields the scattering rate  $S_{\chi=3}^{\text{Absp}}(\mathbf{k}', i'; \mathbf{k}, i)$  and  $S_{\chi=3}^{\text{Emss}}(\mathbf{k}, i; \mathbf{k}', i')$  used in (2.12). As did in (2.13), we can derive the scattering rates for  $E_{\chi=4} = -\hbar \omega_{XX}^{s1}$  by using the relation

$$S_{\chi=4}^{\text{Absp}}(\mathbf{k}', i'; \mathbf{k}, i) = S_{\chi=3}^{\text{Emss}}(\mathbf{k}, i; \mathbf{k}', i'), \quad S_{\chi=4}^{\text{Emss}}(\mathbf{k}, i; \mathbf{k}', i') = S_{\chi=3}^{\text{Absp}}(\mathbf{k}', i'; \mathbf{k}, i).$$

Unlike an optical phonon, the energy of an acoustic phonon is assume to small enough to be ignored. So the AP scattering is regarded as elastic, i.e., the energy of an acoustic phonon is assumed to be  $E_\chi = E_{ac} = 0$ . The scattering rates due to absorbing/emitting an acoustic phonon can be combined into one formula. As a result, the AP scattering only

corresponds to one kind of scattering with  $S_\chi^{\text{Absp}}(\mathbf{k}', i'; \mathbf{k}, i)$  and  $S_\chi^{\text{Emss}}(\mathbf{k}, i; \mathbf{k}', i')$  given as

$$S_\chi^{\text{Absp}}(\mathbf{k}', i'; \mathbf{k}, i) = S_\chi^{\text{Emss}}(\mathbf{k}, i; \mathbf{k}', i') = K_\chi \delta(\mathcal{E}_{i'}(x, \mathbf{k}') - \mathcal{E}_i(x, \mathbf{k})) I_{ii'}(x), \quad (2.16)$$

where

$$K_\chi = \frac{2\pi E_{ac}^2 k_B T}{\hbar \rho_0 u_s^2}, \quad (2.17)$$

$I_{ii'}(x)$  is given in Eq. (2.15b), the deformation potential  $E_{ac}$ , the density of crystal lattice  $\rho_0$  and the acoustic velocity  $u_s$  given in Table 1.

As a summary, we have listed 15 kinds of scattering in this paper with  $\chi=0, 1, 2, \dots, 14$  in (2.11). First,  $\chi=0$  denotes the AP scattering and the scattering rate is given in Eq. (2.16). Then we can use (2.14a) and (2.14b) to calculate the scattering rates of the OP scattering rates and the IOP scattering rates for  $E_\chi > 0$ . Finally we can use the relation (2.13) to give the scattering rates for  $E_\chi < 0$ .

**Remark 2.1.** From Eqs. (2.14a), (2.14b), (2.16) and (2.15b), it can be seen that  $S_\chi^{\text{Absp}}$  and  $S_\chi^{\text{Emss}}$  are functions of the position  $x$ . However, the  $x$  variable dependence has been dropped for brevity.

## 2.2 Nondimensionalization

First we list the physical constants and some numerical values involved in Table 1. Then we introduce the following change of variables to nondimensionalize all the equations and parameters. All the real space length is scaled by  $x_{\text{ref}}$  (given in Table 1), i.e.,

$$\tilde{x} = \frac{x}{x_{\text{ref}}}, \quad \tilde{z} = \frac{z}{x_{\text{ref}}}. \quad (2.18)$$

And the sizes of the device such as  $L$ ,  $L_z$ ,  $L_{SD}$ ,  $L_{Ch}$ ,  $T_{Ox}$  and  $T_{Si}$  are also scaled by  $x_{\text{ref}}$ . The  $|\varphi_{i,x}(z)|^2$  has a unit of  $\text{cm}^{-1}$  and satisfies  $\int_0^{T_{Si}} |\varphi_{i,x}(z)|^2 dz = 1$ , so the adimensional eigen wavefunctions  $\tilde{\varphi}_{i,\tilde{x}}(\tilde{z})$  is related to  $\varphi_{i,x}(z)$  through

$$\tilde{\varphi}_{i,\tilde{x}}(\tilde{z}) = \sqrt{x_{\text{ref}}} \varphi_{i,x}(z). \quad (2.19)$$

All the energy quantities are scaled by the thermal energy  $k_B T$ , i.e.,

$$\tilde{\mathcal{E}}_i(\tilde{t}, \tilde{x}, \tilde{\mathbf{k}}) = \frac{\mathcal{E}_i(t, x, \mathbf{k})}{k_B T}, \quad \tilde{E}_i(\tilde{t}, \tilde{x}) = \frac{E_i(t, x)}{k_B T}, \quad \tilde{E}_\chi = \frac{E_\chi}{k_B T}, \quad (2.20)$$

and the potential is scaled by the thermal voltage  $V_t$

$$\tilde{V}(\tilde{t}, \tilde{x}, \tilde{z}) = \frac{V(t, x, z)}{V_t}. \quad (2.21)$$

The wave vector in the subband  $i$  is scaled by

$$\tilde{k}_x = \frac{\hbar k_x}{\sqrt{m_{x,i} k_B T}}, \quad \tilde{k}_y = \frac{\hbar k_y}{\sqrt{m_{y,i} k_B T}}. \quad (2.22)$$

The time is scaled by  $t_{\text{ref}} = \sqrt{(m_0/k_B T)} x_{\text{ref}} \approx 1.483344 \times 10^{-14} \text{s}$ ,

$$\tilde{t} = \frac{t}{t_{\text{ref}}}. \quad (2.23)$$

The effective masses are scaled by the electron rest mass  $m_0$ ,

$$\tilde{m}_{x,i} = \frac{m_{x,i}}{m_0}, \quad \tilde{m}_{y,i} = \frac{m_{y,i}}{m_0}, \quad \tilde{m}_{z,i} = \frac{m_{z,i}}{m_0}. \quad (2.24)$$

The electron density and the doping density are scaled by  $x_{\text{ref}}^3$ ,

$$\tilde{n}(\tilde{x}, \tilde{z}) = n(x, z) x_{\text{ref}}^3, \quad \tilde{N}_d = N_d x_{\text{ref}}^3. \quad (2.25)$$

The scattering parameter  $K_\chi$  in (2.15a) for the optical phonons and in (2.17) for the acoustic phonons are scaled by  $K_{\text{ref}} = \hbar^2 \sqrt{k_B T} / m_0^{3/2} \approx 5.14258 \times 10^{-9} \text{eVcm}^{-3} \text{s}^{-1}$ ,

$$\tilde{K}_\chi = \frac{K_\chi}{K_{\text{ref}}}. \quad (2.26)$$

The electric permittivity is scaled with

$$\tilde{\epsilon}(\tilde{x}, \tilde{z}) = \frac{x_{\text{ref}} V_t}{q_e} \epsilon(x, z). \quad (2.27)$$

For simplicity, the tilde over the adimensional quantities will be dropped henceforth. Applying the change of variables (2.18), (2.20), (2.19) and (2.21) to Eq. (2.5), we obtain the nondimensionalized Schrödinger equations

$$\left[ -C_{sch} \frac{1}{m_{z,v}} \frac{\partial^2}{\partial z^2} - V(x, z) \right] \varphi_{v,j,x}(z) = E_{v,j,x} \varphi_{v,j,x}(z), \quad z \in (T_{Ox}, T_{Ox} + T_{Si}), \quad (2.28)$$

where  $C_{sch} = \hbar^2 / 2m_0 V_t x_{\text{ref}}^2$ . The total energy (2.6) is written into a nondimensionalized form

$$\mathcal{E}_{v,j}(t, x, \mathbf{k}) = E_{v,j}(t, x) + \omega_v(\mathbf{k}), \quad (2.29)$$

where the dispersion relation (2.7) is reduced into

$$\omega_v(\mathbf{k}) = \frac{1}{2} (k_x^2 + k_y^2). \quad (2.30)$$

Plugging (2.18), (2.21), (2.25) and (2.27) into (2.8) and (2.9), we obtain the nondimensionalized Poisson equation

$$-\nabla_{x,z} \cdot (\epsilon(x,z) \nabla_{x,z} V(t,x,z)) = \begin{cases} N_D(x) - n(x,z), & \text{if } (x,z) \in (0,L) \times (T_{Ox}, T_{Ox} + T_{Si}), \\ 0, & \text{else,} \end{cases} \quad (2.31)$$

where the adimensional electron density  $n(x,z)$  is calculated with

$$n(x,z) = \sum_i n_i(x,z) = \frac{C_n}{2\pi^2} \sum_i \sqrt{m_{x,i} m_{y,i}} \iint_{\mathbb{R}^2} f_i dk_x dk_y |\varphi_i(x,z)|^2, \quad (2.32)$$

with an adimensional constant  $C_n = m_0 k_B T x_{\text{ref}}^2 / \hbar^2 \approx 0.339005$ . Plugging (2.18)-(2.25) into Eqs. (2.1), (2.11) and (2.12), and multiplying  $t_{\text{ref}} = \sqrt{(m_0/k_B T)} x_{\text{ref}}$  on both sides of Eq. (2.1), we obtain the nondimensionalized BTE in the subband  $i$

$$\frac{\partial f_i}{\partial t} + v_i \frac{\partial f_i}{\partial x} + F_i \frac{\partial f_i}{\partial k_x} = \frac{\partial}{\partial t} f_i \Big|_{\text{Scat}}, \quad x \in (0,L), \quad (2.33)$$

where

$$v_i = \frac{1}{\sqrt{m_{x,i}}} \frac{\partial \mathcal{E}_i}{\partial k_x}, \quad (2.34a)$$

$$F_i = -\frac{1}{\sqrt{m_{x,i}}} \frac{\partial \mathcal{E}_i}{\partial x} = -\frac{1}{\sqrt{m_{x,i}}} \frac{\partial E_i}{\partial x}, \quad (2.34b)$$

with the total energy  $\mathcal{E}_i$  given in (2.29). The adimensional scattering term in (2.33) has the same form as (2.11). One typical scattering term (2.12) will be written in the nondimensionalized form

$$\begin{aligned} \frac{\partial f_i}{\partial t} \Big|_{\chi} &= \sum_{i'} \frac{1}{(2\pi)^2} \sqrt{m_{x,i'} m_{y,i'}} \iint_{\mathbb{R}^2} S_{\chi}^{\text{Absp}}(\mathbf{k}', i'; \mathbf{k}, i) f_{i'}(t, x, \mathbf{k}') (1 - f_i(t, x, \mathbf{k})) d^2 \mathbf{k}' \\ &\quad - \sum_{i'} \frac{1}{(2\pi)^2} \sqrt{m_{x,i'} m_{y,i'}} \iint_{\mathbb{R}^2} S_{\chi}^{\text{Emss}}(\mathbf{k}, i; \mathbf{k}', i') f_i(t, x, \mathbf{k}) (1 - f_{i'}(t, x, \mathbf{k}')) d^2 \mathbf{k}', \end{aligned} \quad (2.35)$$

where the scattering rates for OP and IOP scattering have the same form as (2.14a), (2.14b) and (2.15b), and for the AP scattering the same form as (2.16), (2.14b) and (2.15b). But their scattering parameters  $K_{\chi}$  in (2.15a) and (2.17) need to be nondimensionalized by using (2.26). The adimensional  $K_{\chi}$  for the OP/IOP scattering is calculated with

$$K_{\chi} = \frac{\pi D_{\chi}^2}{\rho_0 \omega_{\chi}} \frac{1}{K_{\text{ref}}}, \quad (2.36)$$

where  $(D_{\chi}, \omega_{\chi}) = (D_{op}, \omega_{op})$  in Table 1 or a pair of values listed in Table 2. And the adimensional  $K_{\chi}$  for the AP scattering

$$K_{\chi} = \frac{2\pi E_{ac}^2 k_B T}{\hbar \rho_0 u_s^2} \frac{1}{K_{\text{ref}}}, \quad (2.37)$$

where  $E_{ac}$ ,  $\rho_0$ ,  $u_s$  are listed in Table 1.

### 2.3 The initial value for the time dependent BTE

The Schrödinger equations (2.28) and the Poisson equation (2.31) can be also closed and form a self-consistent Schrödinger-Poisson system if  $f_i$  in the electron density  $n(x,z)$  in (2.32) is given using a simple method instead of solving the time-dependent BTE (2.33).

The first method to determine  $f_i$  in (2.32) is by assuming the electrons in the whole device are in equilibrium with a given Fermi level  $E_F(x)$ , which varies along the transport direction  $x$ ,

$$f_i(x, \mathbf{k}) = \frac{1}{1 + \exp(\mathcal{E}_i(x, \mathbf{k}) - E_F(x))}.$$

When the voltage drop is very slow in the source/drain extension (where the resistivity is low because of high doping density) and the  $V_{DS}$  drop is almost all in the channel region [19], the Fermi level in the device could be approximated with

$$E_F(x) = \begin{cases} E_{F1}, & \text{if } 0 \leq x < L_{SD}, \\ (E_{F2} - E_{F1}) \frac{x - L_{SD}}{L_{Ch}}, & \text{if } L_{SD} \leq x \leq L_{SD} + L_{Ch}, \\ E_{F2}, & \text{if } L_{SD} + L_{Ch} \leq x \leq L. \end{cases}$$

The second method to determine  $f_i$  in (2.32) is to solve a steady ballistic BTE in each subband analytically. The probability distribution function  $f_i(x, \mathbf{k})$  is determined by using the characteristic method [21].  $f_i(x, \mathbf{k}) = (1 + \exp(\mathcal{E}_i(x, \mathbf{k}) - E_{F1}))^{-1}$  if the electron at  $(x, \mathbf{k})$  in the subband  $i$  comes from the source drain, else  $f_i(x, \mathbf{k}) = (1 + \exp(\mathcal{E}_i(x, \mathbf{k}) - E_{F2}))^{-1}$ . When  $V_{GS}$  is very low and  $V_{DS}$  is small, a potential well maybe exists in the channel region. In that case, we can not determine the electrons in the well whether coming from the source contact or the drain contact, so the second method will not work.

The Newton-Raphson method is used to solve the nonlinear Schrödinger-Poisson system [17] with a Jacobian to be determined. A good approximation of the Jacobian (e.g., described in [9]) is used. The Jacobian is estimated by fitting the electron density resulting from Eq. (2.32) with the electron density expression

$$n(x, z) = N_c F_{\frac{1}{2}}((-V(x, z) - \mu(x))),$$

where  $N_c = 12\sqrt{0.916 \times 0.19^2} (m_0 V_t x_{ref}^2 / 2\pi\hbar^2)^{3/2}$  is the adimensional effective density of states,  $F_{1/2}$  is the Fermi-Dirac integral of order 1/2, and  $\mu(x)$  is a fitting parameter (whose value need not to be truly evaluated when finding the approximation of  $\partial n / \partial V$ ). Readers who are interested in using an exact Jacobian in the Newton-Raphson iteration refer to [1].

After the iteration for the self-consistent Schrödinger-Poisson system converges, the subband  $E_i(x)$  and the eigen wavefunction  $\varphi_{i,x}(z)$  are used as the initial values for the time dependent BTEs (2.33). The  $f_i$  obtained either by the first method or by the second method provides the initial probability distribution function for the time dependent BTEs (2.33).

### 3 Numerical schemes

The Boltzmann-Schrödinger-Poisson system consists of Eqs. (2.33) (2.28) and (2.31). Our solver for the complete model contains two blocks. One is the SP-block (Schrödinger-Poisson) by Newton-Raphson iterations. The other is the BTE-block (Boltzmann transport equation). The SP-block is almost the same as the Schrödinger-Poisson solver in Subsection 2.3. The only difference is that when we update electron density during solving the self-consistent Schrödinger-Poisson system, we fix  $f_i$  in (2.32) to be the solution of the BTEs (2.33) at some time  $t$ . A central finite difference method is applied to the Poisson equation and Schrödinger equations. The linear system resulted from the discretization of the Poisson equation is solved by the parallel GMRES method in AztecOO, which provides an object-oriented interface for the well-known Aztec solver library. The eigen problems obtained from Schrödinger equations are solved by STEQR in LAPACK. Trilinos provides a friendly interface for both AztecOO and LAPACK [16].

Henceforth we focus on the BTE-block.

#### 3.1 Reformulate the BTE

Observing the nondimensionalized dispersion relation (2.30), we introduce the coordinate transformation

$$k_x = \sqrt{2\omega} \cos\theta, \quad k_y = \sqrt{2\omega} \sin\theta, \quad (3.1)$$

whose Jacobian is 1. So the variable  $\omega = (k_x^2 + k_y^2)/2$  is the adimensional kinetic energy of the electron with a wave vector  $\mathbf{k} = (k_x, k_y)$ . Comparing (3.1) and the dispersion relation (2.30), we find that  $\omega_v = \omega$  for all the valleys. So the total energy (2.29) is simplified into

$$\mathcal{E}_i(x, \omega, \theta) = E_i(x) + \omega, \quad (3.2)$$

and henceforth the  $\theta$  will be omitted since the total energy does not really depend on  $\theta$ .

Applying the coordinate transformation (3.1), we rewrite the Boltzmann transport equation (2.33) into

$$\frac{\partial}{\partial t} f_i + v_i \frac{\partial f_i}{\partial x} + F_i \left( \sqrt{2\omega} \cos\theta \frac{\partial f_i}{\partial \omega} - \frac{\sin\theta}{\sqrt{2\omega}} \frac{\partial f_i}{\partial \theta} \right) = \frac{\partial f_i}{\partial t} \Big|_{\text{Scat}}, \quad (3.3)$$

where the adimensional  $v_i$  in (2.34a) is expressed with the variables  $\omega$  and  $\theta$

$$v_i = \frac{\sqrt{2\omega} \cos\theta}{\sqrt{m_{x,i}}}, \quad (3.4)$$

and  $F_i$  is the same as (2.34b). By applying the coordinate transformation (3.1) to (2.35), one kind of scattering in the scattering part of Eq. (3.3) is rewritten into

$$\begin{aligned} \frac{\partial f_i}{\partial t} \Big|_{\chi} = & \sum_{i'} \frac{1}{(2\pi)^2} \sqrt{m_{x,i'} m_{y,i'}} \iint_{\mathbb{R}^2} S_{\chi}^{\text{Absp}}(\omega', i'; \omega, i) f_{i'}(t, x, \omega', \theta') (1 - f_i(t, x, \omega, \theta)) d\omega' d\theta' \\ & - \sum_{i'} \frac{1}{(2\pi)^2} \sqrt{m_{x,i'} m_{y,i'}} \iint_{\mathbb{R}^2} S_{\chi}^{\text{Emss}}(\omega, i; \omega', i') f_i(t, x, \omega, \theta) (1 - f_{i'}(t, x, \omega', \theta')) d\omega' d\theta', \end{aligned} \quad (3.5)$$

where the scattering rates do not change with respect to  $\theta$ , so the  $\theta$  variable has been omitted. When we apply the coordinate transformation (3.1) to the scattering rates  $S_\chi^{\text{Absp}}$ , we only need to use the total energy (2.29) and rewrite the  $\delta$ -function in (2.14a) and (2.16) into

$$\delta(\mathcal{E}_{i'}(x, \mathbf{k}') + E_\chi - \mathcal{E}_i(x, \mathbf{k})) \xrightarrow{(3.1)} \delta(\omega' - \omega - \Delta E_{ii'\chi}), \quad (3.6)$$

where  $\Delta E_{ii'\chi}(x) = -E_\chi - E_{i'}(x) + E_i(x)$ . The coordinate transformation (3.1) does not change the relation between  $S_\chi^{\text{Emss}}$  and  $S_\chi^{\text{Absp}}$  expressed in (2.14b).

The computational domain is discretized into a tensor product mesh, and a uniform mesh is taken in the  $x$ -/ $\theta$ -directions and a nonuniform mesh in the  $\omega$ -direction:

$$[0, L] = \bigcup_{j=0}^{N_x-1} [x_{j-\frac{1}{2}}, x_{j+\frac{1}{2}}], \quad x_{j-\frac{1}{2}} = j\Delta x, \quad (3.7)$$

$$[\theta_{\min}, \theta_{\min} + 2\pi] = \bigcup_{l=0}^{N_\theta-1} [\theta_{l-\frac{1}{2}}, \theta_{l+\frac{1}{2}}], \quad \theta_l = -\pi + l\Delta\theta, \quad (3.8)$$

$$[0, \omega_{\max}] = \bigcup_{k=0}^{N_\omega-1} [\omega_{k-\frac{1}{2}}, \omega_{k+\frac{1}{2}}], \quad \omega_{k-\frac{1}{2}} = \frac{1}{2}r_{k-\frac{1}{2}}^2, \quad r_{k-\frac{1}{2}} = \frac{k\sqrt{2\omega_{\max}}}{N_\omega}, \quad (3.9)$$

where  $\Delta x = L/N_x$ ,  $\Delta\theta = 2\pi/N_\theta$ , and we choose  $\theta_{\min} = \theta_{-1/2} = -\pi - \Delta\theta/2$ . The size of the  $k$ 'th  $\omega$ -cell  $\Delta\omega_k = \omega_{k+1/2} - \omega_{k-1/2}$ . In this way the  $\theta$ -domain is  $[-\pi, \pi]$  with a shift  $-\Delta\theta/2$ , but it does not make a difference from choosing the domain  $[0, 2\pi]$  because of the periodicity in the  $\theta$ -domain with a period  $2\pi$ . We use  $[0, \omega_{\max}]$  to replace  $[0, \infty]$  and the choice of  $\omega_{\max}$  depends on the doping density and the bias voltages. In this paper, we choose  $\omega_{\max} = 150$ . Observing Eq. (3.1), we find  $r = \sqrt{2\omega}$  is proportional to the magnitude of the electron momentum. So the  $\omega$ -mesh (3.9) is actually obtained from a uniform  $r$ -mesh on  $[0, \sqrt{2\omega_{\max}}]$ .

### 3.2 The splitting technique

As in [1], we use the splitting technique at two levels:

- Time Splitting (TS), in order to separate the Boltzmann transport equation from scattering, i.e., we split Eq. (3.3) into

$$\frac{\partial}{\partial t} f_i + v_i \frac{\partial f_i}{\partial x} + F_i \left( \sqrt{2\omega} \cos\theta \frac{\partial f_i}{\partial \omega} - \frac{\sin\theta}{\sqrt{2\omega}} \frac{\partial f_i}{\partial \theta} \right) = 0 \quad (3.10)$$

and

$$\frac{\partial}{\partial t} f_i = \frac{\partial f_i}{\partial t} \Big|_{\text{Scat}}. \quad (3.11)$$

- Dimensional splitting (DS), in order to split the  $(x, \omega, \theta)$ -space, i.e., we split Eq. (3.10) into

$$\frac{\partial}{\partial t} f_i + v_i \frac{\partial f_i}{\partial x} = 0 \quad (3.12)$$

and

$$\frac{\partial}{\partial t} f_i + F_i \left( \sqrt{2\omega} \cos\theta \frac{\partial f_i}{\partial \omega} - \frac{\sin\theta}{\sqrt{2\omega}} \frac{\partial f_i}{\partial \theta} \right) = 0. \quad (3.13)$$

The multi-subband BTE is solved by using the splitting technique and is described as follows: Let us suppose that the distribution functions  $f_i(t^n, x, \omega, \theta)$  and the subbands  $E_i(x)$  are known at time  $t^n = n\Delta t$ .

Step 1. Integrate the transport part (3.10) from  $t^n$  to  $t^n + \Delta t/2$ :

I Integration of the  $x$ -advection (3.12) with the initial value (IV)  $f_i(t^n, x, \omega, \theta)$  from  $t^n$  to  $t^n + \Delta t/4$  yields  $f_i^{(1)}(x, \omega, \theta)$ . x-advection:  $\Delta t/4$ .

II Update the electron density by plugging  $f_i^{(1)}(x, \omega, \theta)$  into (2.32). Solve the SP-block to evaluate the subbands  $E_i^*(x)$ .

III Integration of the  $\mathbf{k}$ -advection (3.13) with IV  $f_i^{(1)}(x, \omega, \theta)$  and  $E_i^*(x)$  from  $t^n$  to  $t^n + \Delta t/2$  yields  $f_i^{(2)}(x, \omega, \theta)$ . k-advection:  $\Delta t/2$ .

IV Integration of the  $x$ -advection (3.10) with IV  $f_i^{(2)}(x, \omega, \theta)$  from  $t^n + \Delta t/4$  to  $t^n + \Delta t/2$  yields  $f_i^{(3)}(x, \omega, \theta)$ . x-advection:  $\Delta t/4$ .

Step 2. Update the electron density by plugging  $f_i^{(3)}(x, \omega, \theta)$  into (2.32). Solve the SP-block to evaluate the subbands  $E_i^{**}(x)$  and  $I_{ii'}(x)$  in Eq. (2.15b).

Step 3. Integration of the scattering part (3.11) from  $t^n$  to  $t^n + \Delta t$  with  $E_i^{**}(x)$  and  $I_{ii'}(x)$  obtained in Step 2 and  $f_i(t, x, \omega, \theta) \approx f_i^{(3)}(x, \omega, \theta)$ . Scattering:  $\Delta t$ .

Step 4. Integrate the transport part (3.10) from  $t^n + \Delta t/2$  to  $t^n + \Delta t$  the same way as in Step 1.

The scattering part considered in [1] is a simple relaxation time approximation, so it is not necessary to change  $(k_x, k_y)$  into  $(\omega, \theta)$ . When the electron-phonon scattering is considered, the coordinate transformation (3.1) can facilitate the discretization of the scattering part, but makes the transport part in the wave vector direction complicated. Splitting the  $(\omega, \theta)$ -space into two 1D problems can produce extra dimensional splitting error since Eq. (3.13) is actually a set of 1D problems ( $k_y$  can be regarded as a parameter)

$$\frac{\partial}{\partial t} f_i + F_i \frac{\partial f_i}{\partial k_x} = 0.$$

Thus we do not split the transport in  $(\omega, \theta)$  into two 1D problems but design a numerical scheme for Eq. (3.13) directly using the idea of the PFC method.

### 3.3 Discretization of the transport part in the position space

First, we replace  $v_i$  in (3.12) with the average over the control volume  $\Omega_{kl} = [\omega_{k-1/2}, \omega_{k+1/2}] \times [\theta_{l-1/2}, \theta_{l+1/2}]$ ,

$$v_i(\omega, \theta) \approx v_{ikl} = \frac{1}{\Delta\omega_k \Delta\theta} \int_{\omega_{k-1/2}}^{\omega_{k+1/2}} \int_{\theta_{l-1/2}}^{\theta_{l+1/2}} \frac{\sqrt{2\omega \cos\theta}}{\sqrt{m_{x,i}}} d\omega d\theta.$$

Then we integrate (3.12) over the control volume  $\Omega_{kl}$  and obtain a series of 1D equations

$$\frac{\partial f_{i,kl}(t, x)}{\partial t} + v_{ikl} \frac{\partial f_{i,kl}(t, x)}{\partial x} = 0, \tag{3.14}$$

where  $f_{i,kl}(t, x)$  is the volume average of  $f_i(t, x, \omega, \theta)$  over  $\Omega_{kl}$ ,

$$f_{i,kl}(t, x) = \frac{1}{\Delta\omega_k \Delta\theta} \int_{\omega_{k-1/2}}^{\omega_{k+1/2}} \int_{\theta_{l-1/2}}^{\theta_{l+1/2}} f_i(t, x, \omega, \theta) d\omega d\theta.$$

Remark that  $|v_{ikl}|$  ranges from 0.08432235 to 37.81871 when we use the  $\theta$ -mesh (3.8) with  $N_\theta = 6$  and the  $\omega$ -mesh (3.9) with  $N_\omega = 150$  and  $\omega_{\max} = 150$ . Integration of the ballistic part of the BTE (3.12) from  $t^n$  to  $t^n + \Delta t/4$  requires us to integrate (3.14) with different velocities up to the same time  $t^n + \Delta t/4$ . We use multiple sub-steps with a time step  $\delta t$  to march time from  $t^n$  to  $t^n + \Delta t/4$  for (3.14). We determine  $\delta t$  for Eq. (3.14) with the following rule

$$\delta t = \frac{\Delta x}{\left[ \frac{|v_{ikl}| \Delta t}{4\Delta x} \right] + 1}, \tag{3.15}$$

where  $[a]$  denotes largest integer that is less than or equal to  $a$ . This could help us to get a better accuracy result for Eq. (3.14) with a large velocity, while still allow us to use a big time step  $\delta t$  for (3.14) with a small velocity to reduce the computational cost. Using the time step (3.15), we allow the electron to only move within a distance shorter than  $\Delta x$  in  $\delta t$ , so we can allocate fewer storage space for the exchange of information between different CPUs.

We solve Eq. (3.14) with the PFC method [13,14]. Here we describe how to implement the second order PFC method briefly to a simple transport equation with a constant velocity  $v$

$$\frac{\partial f}{\partial t} + v \frac{\partial f}{\partial x} = 0, \quad x \in [0, L] \tag{3.16}$$

under the condition that the electron moves shorter than  $\Delta x$  in one time step  $\Delta t$ . We can define the characteristic curves solution of the differential system corresponding to the transport equation

$$\begin{cases} \frac{dX(s)}{ds} = v, \\ X(t) = x. \end{cases} \tag{3.17}$$

Let us denote by  $X(s, t, x)$  the solution of (3.17) and define the Jacobian

$$J(s, t, x) = \frac{\partial X(s, t, x)}{\partial x}.$$

In [4], it is proved that if  $J(s, t, x)$  is positive for all  $(s, t, x) \in \mathbb{R}^+ \times \mathbb{R}^+ \times \mathbb{R}$  then the solution of the transport equation (3.16) can be expressed as

$$f(t, x) = f(s, X(s, t, x)) J(s, t, x), \quad (3.18)$$

which describes the conservation of particles along the characteristic curves

$$\forall K \subset \mathbb{R}, \quad \int_K f(t, x) dx = \int_{X(s, t, K)} f(s, x) dx, \quad (3.19)$$

where

$$X(s, t, K) = \{y \in \mathbb{R} : y = X(s, t, z); z \in K\}.$$

This property remains true for higher dimensions than 1. Using the  $x$ -mesh (3.7) and assuming the values of the distribution function are known at time  $t^n = n\Delta t$ , we find the new values at time  $t^{n+1}$  by integration of the distribution function on each cell  $[x_{j-1/2}, x_{j+1/2}]$ . Thus, using the conservation of particles (3.19) and recalling that the solution of (3.17) is  $X(s, t, x) = v(s-t) + x$ , and the Jacobian function  $x \mapsto J(t^n, t^{n+1}, x)$  is 1, we have

$$\int_{x_{j-1/2}}^{x_{j+1/2}} f(t^{n+1}, x) dx = \int_{X(t^n, t^{n+1}, x_{j-1/2})}^{X(t^n, t^{n+1}, x_{j+1/2})} f(t^n, x) dx.$$

Then, we set

$$\Phi_{j+1/2}(t^n) = \int_{X(t^n, t^{n+1}, x_{j+1/2})}^{x_{j+1/2}} f(t^n, x) dx$$

to finally obtain the conservative scheme

$$\int_{x_{j-1/2}}^{x_{j+1/2}} f(t^{n+1}, x) dx = \Phi_{j-1/2}(t^n) + \int_{x_{j-1/2}}^{x_{j+1/2}} f(t^n, x) dx - \Phi_{j+1/2}(t^n). \quad (3.20)$$

The main step is now to choose an efficient method to reconstruct the distribution function from the values  $f_j^n, j=0, \dots, N_x-1$ , which have been obtained. We use  $f_j^n$  to denote the average of the solution  $f(t^n, x)$  over  $[x_{j-1/2}, x_{j+1/2}]$ . We take  $v > 0$  as an example to show how to do the reconstruction. The second-order approximation is obtained by using a linear interpolation to approximate the distribution function  $f(t^n, x)$  in  $[x_{j-1/2}, x_{j+1/2}]$

$$f_h(t^n, x) = f_j^n + \epsilon_j^n (x - x_j) \frac{f_{j+1}^n - f_j^n}{\Delta x}, \quad \forall x \in [x_{j-1/2}, x_{j+1/2}], \quad (3.21)$$

where the slope corrector is introduced to ensure the preservation of positivity and the maximum principle [14]

$$\epsilon_j^n = \begin{cases} \min \left\{ 1, \frac{2f_j^n}{(f_{j+1}^n - f_j^n)} \right\}, & \text{if } f_{j+1}^n > f_j^n, \\ \min \left\{ 1, -\frac{2(f_\infty^n - f_j^n)}{(f_{j+1}^n - f_j^n)} \right\}, & \text{if } f_{j+1}^n < f_j^n. \end{cases} \quad (3.22)$$

Here we denote  $f_\infty^n = \max\{f_j^n : j = 0, \dots, N_x - 1\}$ . It is easy to verify that with the slope corrector (3.22), the reconstructed  $f_h(t^n, x)$ , (3.21) satisfies that  $0 \leq f_h(t^n, x) \leq f_\infty^n$ ,  $x \in [0, L]$ . Then we can define an approximation of  $\Phi_j(t^n)$

$$\Phi_{j+\frac{1}{2}}(t^n) = v\Delta t \left[ f_j^n + \frac{\epsilon_j^n}{2} \left( 1 - \frac{v\Delta t}{\Delta x} \right) (f_{j+1}^n - f_j^n) \right].$$

For  $v > 0$ , we use an inflow boundary condition, i.e.,  $f(t, x=0)$  is a given function of  $t$ . So the boundary condition at  $x=0$  is clear. But  $f(t, x)$ ,  $x=L$  is not given. When we use the linear interpolation (3.21) at  $[x_{N_x-3/2}, x_{N_x-1/2}]$ , we need to use  $f_{N_x}^n$ . So we set  $f_{N_x}^n$  by a linear interpolation

$$f_{N_x}^n = 2f_{N_x-1}^n - f_{N_x-2}^n.$$

### 3.4 Discretization of the transport part in the wave vector space

With the help of the dimensional splitting, the transport equation (3.13) in the  $(\omega, \theta)$ -space in different cells  $[x_{j-1/2}, x_{j+1/2}]$  can be solved independently. We approximate  $F_i$  in  $[x_{j-1/2}, x_{j+1/2}]$  by

$$F_{i,j} = -\frac{E_i(x_{j+1}) - E_i(x_{j-1})}{2\Delta x \sqrt{m_{x,i}}}$$

using a central finite difference scheme to discretize (2.34b). The integration of Eq. (3.13) over  $[x_{j-1/2}, x_{j+1/2}]$  yields a series of simple 2D transport equations

$$\frac{\partial f_{i,j}(t, \omega, \theta)}{\partial t} + F_{i,j} \left( \sqrt{2\omega} \cos \theta \frac{\partial f_{i,j}(t, \omega, \theta)}{\partial \omega} - \frac{\sin \theta}{\sqrt{2\omega}} \frac{\partial f_{i,j}(t, \omega, \theta)}{\partial \theta} \right) = 0, \quad (3.23)$$

where  $f_{i,j}(t, \omega, \theta)$  is the average of the distribution function  $f_i(t, x, \omega, \theta)$  over  $[x_{j-1/2}, x_{j+1/2}]$ ,

$$f_{i,j}(t, \omega, \theta) = \frac{1}{\Delta x} \int_{x_{j-\frac{1}{2}}}^{x_{j+\frac{1}{2}}} f_i(t, x, \omega, \theta) dx. \quad (3.24)$$

The integration of Eq. (3.13) from  $t^n$  to  $t^n + \Delta t/2$  requires us to integrate (3.23) in each cell  $[x_{j-1/2}, x_{j+1/2}]$  up to  $t^n + \Delta t/2$ . We use multiple sub-steps with a time step  $\delta t$  for (3.23) to march from  $t^n$  to  $t^n + \Delta t/2$ .  $\delta t$  maybe be very small in a cell  $[x_{j-1/2}, x_{j+1/2}]$  if the force  $F_{i,j}$

is very big. Using the meshes given in (3.8) and (3.9), we determine  $\delta t$  for Eq. (3.23) with a force  $F_{i,j}$  by

$$\delta t < \min \left\{ \frac{\sqrt{2\omega_{1/2}} \tan \Delta \theta}{|F_{i,j}|}, \frac{\sqrt{2\omega_{\max}}}{N\omega |F_{i,j}|}, \frac{\Delta t}{2} \right\}. \quad (3.25)$$

In order to show how to solve (3.23), we just need to give the numerical scheme for a simple 2D equation

$$\frac{\partial f(t, \omega, \theta)}{\partial t} + F \left( \sqrt{2\omega} \cos \theta \frac{\partial f(t, \omega, \theta)}{\partial \omega} - \frac{\sin \theta}{\sqrt{2\omega}} \frac{\partial f(t, \omega, \theta)}{\partial \theta} \right) = 0, \quad (3.26)$$

or its equivalent form in  $(k_x, k_y)$

$$\frac{\partial f(t, k_x, k_y)}{\partial t} + F \frac{\partial f(t, k_x, k_y)}{\partial k_x} = 0, \quad (3.27)$$

where  $F$  is a constant positive force. We give a numerical scheme for (3.26) with a time step  $\Delta t$  which satisfies

$$\Delta t < \min \left\{ \frac{\sqrt{2\omega_{1/2}} \tan \Delta \theta}{F}, \frac{\sqrt{2\omega_{\max}}}{N\omega F} \right\}. \quad (3.28)$$

As done for (3.16), we can define the characteristic curves of (3.27) the solution of

$$\begin{cases} \frac{d\mathbf{K}(s)}{ds} = (F, 0), \\ \mathbf{K}(t) = (k_x, k_y), \end{cases} \quad (3.29)$$

where  $\mathbf{K} = (K_x, K_y)$ . Let us denote  $\mathbf{K}(s, t, (k_x, k_y))$  the solution of (3.29) and define the Jacobian

$$J(s, t, (k_x, k_y)) = \begin{vmatrix} \frac{\partial K_x}{\partial k_x} & \frac{\partial K_x}{\partial k_y} \\ \frac{\partial K_y}{\partial k_x} & \frac{\partial K_y}{\partial k_y} \end{vmatrix}.$$

It is easy to see that  $K_x(s, t, (k_x, k_y)) = k_x + F(s - t)$ ,  $K_y = k_y$  and  $J(s, t, (k_x, k_y)) = 1$ . The characteristic curves of (3.26) can be obtained by using the characteristics of (3.27) through the coordinate transformation (3.1) which can be written into

$$(k_x, k_y) = \mathbf{G}(\omega, \theta). \quad (3.30)$$

But we do not really need to write out the expression of the characteristic curves of (3.26). Using the 2D counterpart of the conservation of particles (3.19), we have

$$\iint_{\Omega_{kl}} f(t^{n+1}, \omega, \theta) d\omega d\theta = \iint_{\tilde{\Omega}(t^n, t^{n+1}, \Omega_{kl})} f(t^n, \omega, \theta) d\omega d\theta, \quad (3.31)$$

where we use the  $\omega$ -mesh (3.9) and the  $\theta$ -mesh (3.8) and denote  $\Omega_{kl} = [\omega_{k-1/2}, \omega_{k+1/2}] \times [\theta_{l-1/2}, \theta_{l+1/2}]$  and

$$\tilde{\Omega}(t^n, t^{n+1}, \Omega_{kl}) = \left\{ G^{-1}(\mathbf{K}(t^n, t^{n+1}, G(\omega, \theta))) : (\omega, \theta) \in \Omega_{kl} \right\}. \quad (3.32)$$

We will denote  $\tilde{\Omega}(t^n, t^{n+1}, \Omega_{kl})$  by  $\tilde{\Omega}_{kl}$ . Recalling that the Jacobian of the coordinate transformation (3.30) is 1, we have

$$\iint_{\Omega_{kl}} f(t^{n+1}, \omega, \theta) d\omega d\theta = \iint_{G(\Omega_{kl})} f(t^{n+1}, k_x, k_y) dk_x dk_y, \quad (3.33)$$

where we denote

$$G(\Omega_{kl}) = \{ G(\omega, \theta) : (\omega, \theta) \in \Omega_{kl} \},$$

and

$$f(t^{n+1}, k_x, k_y) \triangleq f(t^{n+1}, \omega(k_x, k_y), \theta(k_x, k_y)).$$

We plot  $G(\Omega_{kl})$  and  $G(\tilde{\Omega}_{kl})$  in Fig. 2. Using the notations in Fig. 2, we can set

$$\Phi_{k, l+\frac{1}{2}}(t^n) = \iint_{G^{-1}(A'_{(k-1/2)(l+1/2)} A_{(k-1/2)(l+1/2)} A_{(k+1/2)(l+1/2)} A'_{(k+1/2)(l+1/2)})} f(t^n, \omega, \theta) d\omega d\theta \quad (3.34a)$$

and

$$\Phi_{k+\frac{1}{2}, l}(t^n) = \iint_{G^{-1}(A'_{(k+1/2)(l-1/2)} A_{(k+1/2)(l-1/2)} A_{(k+1/2)(l+1/2)} A'_{(k+1/2)(l+1/2)})} f(t^n, \omega, \theta) d\omega d\theta. \quad (3.34b)$$

Thus, we finally obtain the conservative scheme for (3.26)

$$\begin{aligned} \iint_{\Omega_{kl}} f(t^{n+1}, \omega, \theta) d\omega d\theta &= \iint_{\Omega_{kl}} f(t^n, \omega, \theta) d\omega d\theta + \Phi_{k, l-\frac{1}{2}}(t^n) - \Phi_{k, l+\frac{1}{2}}(t^n) \\ &\quad + \Phi_{k-\frac{1}{2}, l}(t^n) - \Phi_{k+\frac{1}{2}, l}(t^n). \end{aligned} \quad (3.35)$$

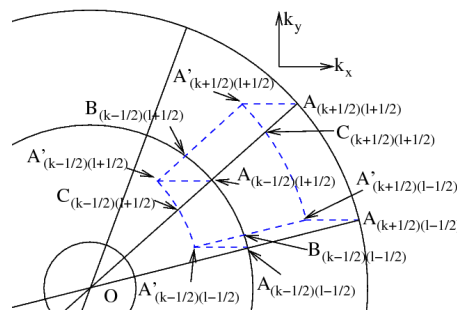


Figure 2:  $A_{(k-1/2)(l-1/2)} = G(\omega_{k-1/2}, \theta_{l-1/2})$ .  $A'_{(k-1/2)(l-1/2)} = \mathbf{K}(t^n, t^{n+1}, A_{(k-1/2)(l-1/2)})$ .  $A_{(k-1/2)(l-1/2)} A_{(k+1/2)(l-1/2)} A_{(k+1/2)(l+1/2)} A_{(k-1/2)(l+1/2)}$  is  $G(\Omega_{kl})$ , and  $A'_{(k-1/2)(l-1/2)} A'_{(k+1/2)(l-1/2)} A'_{(k+1/2)(l+1/2)} A'_{(k-1/2)(l+1/2)}$  is  $G(\tilde{\Omega}_{kl})$ .

We denote

$$f_{kl}^n = \frac{1}{\Delta\omega_k \Delta\theta} \iint_{\Omega_{kl}} f(t^n, \omega, \theta) d\omega d\theta.$$

Up to now, the last step to complete the numerical scheme is to reconstruct a piecewise linear distribution function from the values  $f_{kl}^n$ ,  $k = 0, \dots, N_\omega - 1$ ,  $l = 0, \dots, N_\theta - 1$ , which have been obtained at time  $t^n$ . The ENO reconstruction seems to be useful in solving the Vlasov equation because though it does not develop any shock, stiff gradients appear in the phase space [14]. We choose the stencil like the ENO reconstruction. In order to reconstruct the linear function in  $\Omega_{kl}$ , we add  $\Omega_{k+1,l}$  to the stencil if

$$\frac{|f_{(k+1)l}^n - f_{kl}^n|}{\Delta\omega_{k+1} + \Delta\omega_k} < \frac{|f_{kl}^n - f_{(k-1)l}^n|}{\Delta\omega_k + \Delta\omega_{k-1}},$$

otherwise  $\Omega_{(k-1)l}$ . We use the same way to add either  $\Omega_{k(l+1)}$  or  $\Omega_{k(l-1)}$  to the stencil. In the sequel, we suppose that  $\{\Omega_{kl}, \Omega_{(k+1)l}, \Omega_{k(l+1)}\}$  is the chosen stencil.  $t^n$  and  $n$  will be dropped henceforth for brevity since all will be done at time  $t^n$ . First, a linear interpolation reconstruction in  $\Omega_{kl}$  can be given as

$$f_h(\omega, \theta) = f_{kl} + \frac{2(f_{(k+1)l} - f_{kl})}{\Delta\omega_{k+1} + \Delta\omega_k} (\omega - \omega_k) + \frac{f_{k(l+1)} - f_{kl}}{\Delta\theta} (\theta - \theta_l), \quad (\omega, \theta) \in \Omega_{kl}. \quad (3.36)$$

But this approximation may not ensure the maximum principle:  $0 \leq f_h(\omega, \theta) < f_\infty$ , where

$$f_\infty = \max \{f_{kl} : k = 0, \dots, N_\omega - 1, l = 0, \dots, N_\theta - 1\}.$$

We introduce the two slope correctors  $\epsilon_{\omega,kl}$  and  $\epsilon_{\theta,kl}$  with a two step method. The first step is to set

$$\epsilon_{\omega,kl}^{(1)} = \begin{cases} \min \left\{ 1, \frac{f_{kl}}{f_{(k+1)l} - f_{kl}} \frac{\Delta\omega_k + \Delta\omega_{k+1}}{\Delta\omega_k} \right\}, & \text{if } f_{(k+1)l} > f_{kl}, \\ \min \left\{ 1, -\frac{f_\infty - f_{kl}}{f_{(k+1)l} - f_{kl}} \frac{\Delta\omega_k + \Delta\omega_{k+1}}{\Delta\omega_k} \right\}, & \text{if } f_{(k+1)l} < f_{kl}, \end{cases}$$

$$\epsilon_{\theta,kl}^{(1)} = \begin{cases} \min \left\{ 1, \frac{2f_{kl}}{f_{k(l+1)} - f_{kl}} \right\}, & \text{if } f_{k(l+1)} > f_{kl}, \\ \min \left\{ 1, -\frac{2(f_\infty - f_{kl})}{f_{k(l+1)} - f_{kl}} \right\}, & \text{if } f_{k(l+1)} < f_{kl}. \end{cases}$$

And in the second step we set

$$\epsilon_{kl}^{(2)} = \begin{cases} \min \left\{ 1, \frac{2f_{kl}}{\epsilon_{\theta,kl}^{(1)} |f_{k(l+1)} - f_{kl}| \frac{2\Delta\omega_k}{\Delta\omega_k + \Delta\omega_{k+1}} + \epsilon_{\omega,kl}^{(1)} |f_{k(l+1)} - f_{kl}|} \right\}, & \text{if } 2f_{kl} < f_\infty, \\ \min \left\{ 1, \frac{2(f_\infty - f_{kl})}{\epsilon_{\theta,kl}^{(1)} |f_{k(l+1)} - f_{kl}| \frac{2\Delta\omega_k}{\Delta\omega_k + \Delta\omega_{k+1}} + \epsilon_{\omega,kl}^{(1)} |f_{k(l+1)} - f_{kl}|} \right\}, & \text{if } 2f_{kl} \geq f_\infty. \end{cases}$$

Using these two steps, we obtain two slope correctors

$$\epsilon_{\omega,kl} = \epsilon_{\omega,kl}^{(1)} \epsilon_{kl}^{(2)}, \quad \epsilon_{\theta,kl} = \epsilon_{\theta,kl}^{(1)} \epsilon_{kl}^{(2)}. \quad (3.37)$$

By applying the two slope correctors (3.37), we have modified the linear approximation (3.36) into a reconstruction that ensures the maximum principle

$$f_h(\omega, \theta) = f_{kl} + (\partial_{\omega} f)_{kl}(\omega - \omega_k) + (\partial_{\theta} f)_{kl}(\theta - \theta_l), \quad (\omega, \theta) \in \Omega_{kl}, \quad (3.38)$$

where

$$(\partial_{\omega} f)_{kl} = \epsilon_{\omega,kl} \frac{2(f_{(k+1)l} - f_{kl})}{\Delta\omega_{k+1} + \Delta\omega_k}, \quad (\partial_{\theta} f)_{kl} = \epsilon_{\theta,kl} \frac{f_{k(l+1)} - f_{kl}}{\Delta\theta}.$$

The evaluation of the conservation scheme (3.35) by plugging (3.38) into (3.34a) and (3.34b). The calculation of the fluxes (3.34a) and (3.34b) is more complicated than 1D fluxes. But the fact that the force is only nonzero in the  $x$ -direction makes this task easier than it looks. In addition, the computational cost can be reduced by using symmetry of the  $\theta$ -mesh (3.8). We take a boundary of the control volume  $\Omega_{kl}$  in Fig. 2 as an example to show how to calculate the numerical flux. Since the time step is small (see (3.28)) and we have assumed that the force  $F$  is positive,

$$A'_{(k-1/2)(l+1/2)} A_{(k-1/2)(l+1/2)} A_{(k+1/2)(l+1/2)} A'_{(k+1/2)(l+1/2)}$$

in (3.34a) can only have a nonempty intersection with  $\Omega_{(k-1)(l+1)}$  and  $\Omega_{k(l+1)}$ . Then the flux  $\Phi_{k,l+1/2}$  defined in (3.34a) can be calculated by

$$\Phi_{k,l+\frac{1}{2}} = - \left( \Phi_{k,l+\frac{1}{2}}^{(k-1)(l+1)} + \Phi_{k,l+\frac{1}{2}}^{k(l+1)} \right), \quad (3.39)$$

where “-” comes from the sign of  $-F \sin(\theta_{l+1/2}) / \sqrt{2\omega}$  ( $\theta_{l+1/2}$  in Fig. 2 is in the first quadrant) in (3.26), and

$$\begin{aligned} & \Phi_{k,l+\frac{1}{2}}^{(k-1)(l+1)} \\ &= f_{(k-1)(l+1)} \iint_{A'_{(k-1/2)(l+1/2)} A_{(k-1/2)(l+1/2)} B_{(k-1/2)(l+1/2)}} dk_x dk_y \\ & \quad + (\partial_{\omega} f)_{(k-1)(l+1)} \iint_{A'_{(k-1/2)(l+1/2)} A_{(k-1/2)(l+1/2)} B_{(k-1/2)(l+1/2)}} (\omega(k_x, k_y) - \omega_{k-1}) dk_x dk_y \\ & \quad + (\partial_{\theta} f)_{(k-1)(l+1)} \iint_{A'_{(k-1/2)(l+1/2)} A_{(k-1/2)(l+1/2)} B_{(k-1/2)(l+1/2)}} (\theta(k_x, k_y) - \theta_l) dk_x dk_y, \end{aligned} \quad (3.40a)$$

$$\begin{aligned} & \Phi_{k,l+\frac{1}{2}}^{k(l+1)} \\ &= f_{k(l+1)} \iint_{B_{(k-1/2)(l+1/2)} A_{(k-1/2)(l+1/2)} A_{(k+1/2)(l+1/2)} A'_{(k+1/2)(l+1/2)}} dk_x dk_y \\ & \quad + (\partial_{\omega} f)_{k(l+1)} \iint_{B_{(k-1/2)(l+1/2)} A_{(k-1/2)(l+1/2)} A_{(k+1/2)(l+1/2)} A'_{(k+1/2)(l+1/2)}} (\omega(k_x, k_y) - \omega_k) dk_x dk_y \\ & \quad + (\partial_{\theta} f)_{k(l+1)} \iint_{B_{(k-1/2)(l+1/2)} A_{(k-1/2)(l+1/2)} A_{(k+1/2)(l+1/2)} A'_{(k+1/2)(l+1/2)}} (\theta(k_x, k_y) - \theta_l) dk_x dk_y. \end{aligned} \quad (3.40b)$$

It is convenient for some integrals to be obtained if we introduce the following coordinate transformation

$$k_x = r \cos \theta, \quad k_y = r \sin \theta \tag{3.41}$$

which transforms the rectangular coordinate  $(k_x, k_y)$  to the polar coordinate  $(r, \theta)$ . Comparing the coordinate transform (3.1) and (3.41), we know that for given  $(k_x, k_y)$ ,  $\theta$  in (3.1) and in (3.41) have the same value and

$$r(k_x, k_y) = \sqrt{2\omega(k_x, k_y)}.$$

The given  $\omega$ -mesh (3.9) is a uniform  $r$ -mesh with an  $r$ -mesh size  $\Delta r = \sqrt{2\omega_{\max}}/N_\omega$ . In the polar coordinate, the equation for the line  $A'_{(k-1/2)(l+1/2)}A_{(k-1/2)(l+1/2)}$  is

$$r(\theta) = \frac{r_{k-\frac{1}{2}} \sin \theta_{l+\frac{1}{2}}}{\sin \theta},$$

for the line  $A'_{(k-1/2)(l+1/2)}A'_{(k+1/2)(l+1/2)}$

$$r(\theta) = \frac{F \Delta t \sin \theta_{l+\frac{1}{2}}}{\sin(\theta - \theta_{l+\frac{1}{2}})},$$

and for the shifted circle containing  $A'_{(k-1/2)(l-1/2)}A'_{(k-1/2)(l+1/2)}$

$$r(\theta) = \sqrt{\omega_{k-\frac{1}{2}}^2 - (F \Delta t \sin \theta)^2} - F \Delta t \cos \theta.$$

Using the fact that

$$|A'_{(p-1/2)(q+1/2)}A_{(p-1/2)(q+1/2)}| = F \Delta t, \quad 0 \leq p \leq N_\omega, \quad 0 \leq q < N_\theta,$$

we have

$$\begin{aligned} \iint_{A'_{(k-1/2)(l+1/2)}A_{(k-1/2)(l+1/2)}A_{(k+1/2)(l+1/2)}A'_{(k+1/2)(l+1/2)}} dk_x dk_y &= F \Delta t \Delta r \sin(\theta_{l+\frac{1}{2}}), \\ \iint_{A'_{(k+1/2)(l-1/2)}A_{(k+1/2)(l-1/2)}A_{(k+1/2)(l+1/2)}A'_{(k+1/2)(l+1/2)}} dk_x dk_y &= F \Delta t r_{k+\frac{1}{2}} (\sin(\theta_{l+\frac{1}{2}}) - \sin(\theta_{l-\frac{1}{2}})). \end{aligned}$$

The other integrals involved can be obtained analytically or numerically. For example, we give the following two integrals:

$$\begin{aligned} &\iint_{A'_{(k-1/2)(l+1/2)}A_{(k-1/2)(l+1/2)}B_{(k-1/2)(l+1/2)}} dk_x dk_y \\ &= \omega_{k-\frac{1}{2}} (\arcsin(F_{k-\frac{1}{2}, \Delta t} \sin(\theta_{l+\frac{1}{2}})) + G_0(\theta_{l+\frac{1}{2}}, F_{k-\frac{1}{2}, \Delta t}) - F_{k-\frac{1}{2}, \Delta t} \sin(\theta_{l+\frac{1}{2}})), \\ &\iint_{A'_{(k+1/2)(l+1/2)}C_{(k+1/2)(l+1/2)}A_{(k+1/2)(l+1/2)}} dk_x dk_y \\ &= \omega_{k-\frac{1}{2}} (\arcsin(F_{k+\frac{1}{2}, \Delta t} \sin(\theta_{l+\frac{1}{2}})) + G_1(\theta_{l+\frac{1}{2}}, F_{k-\frac{1}{2}, \Delta t}) - G_1(\bar{\theta}_{(k+\frac{1}{2})(l+\frac{1}{2})}, F_{k-\frac{1}{2}, \Delta t})), \end{aligned}$$

where

$$F_{k-\frac{1}{2},\Delta t} = \frac{F\Delta t}{\sqrt{2\omega_{k-\frac{1}{2}}}}, \quad \bar{\theta}_{(k+\frac{1}{2})(l+\frac{1}{2})} = \arctan\left(\frac{\sin\theta_{l+\frac{1}{2}}}{\cos\theta_{l+\frac{1}{2}} - F_{k-\frac{1}{2},\Delta t}}\right),$$

and

$$G_0(\theta, \zeta) = \zeta \sin\theta \left(1 - \zeta \cos\theta - \sqrt{1 - (\zeta \sin\theta)^2}\right),$$

$$G_1(\theta, \zeta) = \zeta^2 \theta + \frac{1}{2} \zeta^2 \sin(2\theta) - \arcsin(\zeta\theta) - \zeta \arcsin(\theta) \sqrt{1 - (\zeta \sin\theta)^2}.$$

We have shown how to calculate the numerical flux flowing through one of the boundaries of a control volume  $\Omega_{kl}$  in the first quadrant. The other numerical flux can be done in the same way. But we need pay a little more attention to the control volume  $\Omega_{kl}$ , when  $k = 0$  or  $\theta_{l\pm 1/2} = \pm\pi/2$ , because the calculation of the flux may involve more than two control volumes.

$\omega_{\max}$  is assumed to be big enough, so we set  $f_{kl} = 0$ , if  $k \geq N_\omega$ . When we reconstruct a linear function for a control volume  $\Omega_{0l}$ , we need to use  $f_{(-1)l}$ , the average of the distribution function over  $\Omega_{(-1)l}$ . This is related to the boundary conditions at  $\omega = 0$ , which is not really a physical boundary. A "ghost point"  $(\omega, \theta)$  for a negative  $\omega$  is actually a physical point at  $(-\omega, \theta + \pi)$ . So we set

$$f_{(-1)l} = f_{0(l+N_\theta/2)}.$$

We use the periodic boundary condition in the  $\theta$ -space, i.e.,

$$f_{kl} = f_{k(l+N_\theta)}.$$

### 3.5 Discretization of the scattering part

Observing Eqs. (3.5), (2.14a) and (3.6), we know that all the discretization of the scattering integrals can be done in the same way as for

$$\int_0^{\omega_{\max}} \int_{\theta_{\min}}^{\theta_{\min}+2\pi} \delta(\omega' - \omega - \Delta E_{ii'\chi}) f_{i'}(x, \omega', \theta') (1 - f_i(x, \omega, \theta)) d\omega' d\theta', \quad (3.42)$$

where  $f_i(x, \omega, \theta)$  is the distribution function obtained at some time  $t$ . First we obtain the average of (3.42) over a cell  $[x_{j-1/2}, x_{j+1/2}]$

$$\int_0^{\omega_{\max}} \int_{\theta_{\min}}^{\theta_{\min}+2\pi} \delta(\omega' - \omega - \Delta E_{ii'\chi}) f_{i'j}(\omega', \theta') (1 - f_{ij}(\omega, \theta)) d\omega' d\theta', \quad (3.43)$$

where

$$f_{ij}(\omega, \theta) = \frac{1}{\Delta x} \int_{x_{j-\frac{1}{2}}}^{x_{j+\frac{1}{2}}} f_i(x, \omega, \theta),$$

$\omega_{\max}$  in (3.9) and  $\theta_{\min}$  in (3.8). Then we integrate (3.43) over a control volume  $\Omega_{kl} = [\omega_{k-1/2}, \omega_{k+1/2}] \times [\theta_{l-1/2}, \theta_{l+1/2}]$ , then divide it by  $|\Omega_{kl}| = \Delta\omega_k \Delta\theta$ , finally we obtain

$$\frac{1}{|\Omega_{kl}|} \iint_{\Omega_{kl}} d\omega d\theta \int_0^{\omega_{\max}} \int_{\theta_{\min}}^{\theta_{\min}+2\pi} \delta(\omega' - \omega - \Delta E_{ii'\chi}) f_{i'j}(\omega', \theta') (1 - f_{ij}(\omega, \theta)) d\omega' d\theta'. \quad (3.44)$$

Using the property of  $\delta$ -function, we approximate (3.44) with

$$\sum_{k'} \sum_{i'} \xi_{k'k}^{ii'\chi} \sum_{l'} f_{i'j,k'l'} (1 - f_{ij,kl}) \Delta\theta, \quad (3.45)$$

where

$$f_{i'j,kl} = \frac{1}{\Delta\omega_k \Delta\theta} \iint_{\Omega_{kl}} f_{i'j}(\omega, \theta) d\omega d\theta \quad (3.46)$$

and

$$\xi_{k'k}^{ii'\chi} = \frac{|[\omega_{k'-1/2}, \omega_{k'+1/2}] \cap [\omega_{k-1/2} + \Delta E_{ii'\chi}, \omega_{k+1/2} + \Delta E_{ii'\chi}] \cap [0, \omega_{\max}]|}{\Delta\omega_k}. \quad (3.47)$$

Here  $|[\omega_a, \omega_b]|$  is the measure of the set  $[\omega_a, \omega_b]$ . We use  $\cap [0, \omega_{\max}]$  in (3.47) to restrict the electron can only have an energy in the range of  $[0, \omega_{\max}]$ . That is, we assume the probability that an electron absorbs a phonon to gain an energy higher than  $\omega_{\max}$  is zero. When  $\omega_{\max}$  is set to be big enough, this assumption is reasonable. It is easy to see that the numerical scheme (3.45) preserves the conservation of electrons.

## 4 Numerical results and discussion

In this section, we use physical units for a better understanding of the numerical results. We simulate a  $L_{Ch} = 9\text{nm}$  gate length DG MOSFET with a body thickness  $T_{Si} = 3\text{nm}$  and source/drain doping of  $N_{SD} = 10^{20}\text{cm}^{-3}$ . The channel region is intrinsic silicon with  $N_b = 10^{10}\text{cm}^{-3}$ . The channel junctions are abrupt and no Gate-to-S/D overlap is assumed. The effective oxide thickness (EOT) is  $T_{Ox} = 0.5\text{nm}$ . And the length of the source/drain is  $L_{SD} = 9.9\text{nm}$ . The number of the eigenvalues for Schrödinger equation with  $m_z = 0.916m_0$  is chosen to be 2, and for  $m_z = 0.19m_0$  is chose to be 1. So the number of all subbands we calculate is  $N_{\text{subband}} = 2 \times 2 + 1 \times 4 = 8$ . When the lower/upper gates of a DG MOSFET have the same bias voltage, i.e.,  $V_{G_dS} = V_{G_gS}$ , the device is called a symmetric DG MOSFET, otherwise asymmetric. In our code,  $N_{\text{scat}} = 0$  denotes the ballistic case, and  $N_{\text{scat}} = 15$  denotes the transport with both the intra-valley and the inter-valley scattering. We use the meshes with  $\Delta x = 0.3\text{nm}$ ,  $\Delta z = 0.1\text{nm}$ , and  $N_\omega = 150$ . The  $\omega_{\max}$  is chosen to be  $3.879\text{eV}$ , which is big enough for the bias voltage  $V_{DS} \leq 0.5\text{V}$ .

We solve the time-dependent BSP until the stationary state. We use two stopping criteria. The first stopping criteria is on the current oscillation

$$\frac{\max_{0 < j < N_x} I_{j+\frac{1}{2}} - \min_{0 < j < N_x} I_{j+\frac{1}{2}}}{\max_{1 < j < N_x} |I_{j+\frac{1}{2}}|} < 10^{-3},$$

where  $I_{j+1/2}$  is the current at the interface  $x_{j+1/2}$ . When the source-drain current is small because of low  $V_{DS}/V_{GS}$ , the first stopping criteria may not be met. In this case, we use the second stopping criteria that checks the difference of the potential between two time steps

$$|V^{n+1}(x,z) - V^n(x,z)|_{\infty} < 10^{-8}V.$$

#### 4.1 Distribution function in the first subband and surface charge density along the channel direction

In this subsection, we study a symmetric DG MOSFET with  $V_{G_{iS}} = V_{G_{dS}} = 0.3V$ . We discuss the shape of the probability distribution function (pdf) of the lowest subband  $f_0(x, k_x, k_y)$  of the stationary state at different locations along the channel under high drain bias  $V_{DS} = 0.5V$ . We choose four locations to represent substantial changes: the source extension  $x = 3nm$ , the peak position of the first subband  $x_{top} = 10.5nm$ , the middle point of the channel  $x = 14.4nm$ , and the drain extension  $x = 25.4nm$ .

Fig. 3 shows  $f_0(x, k_x, k_y)$  with  $N_{scat} = 0$ , which means ballistic transport. Fig. 4 shows

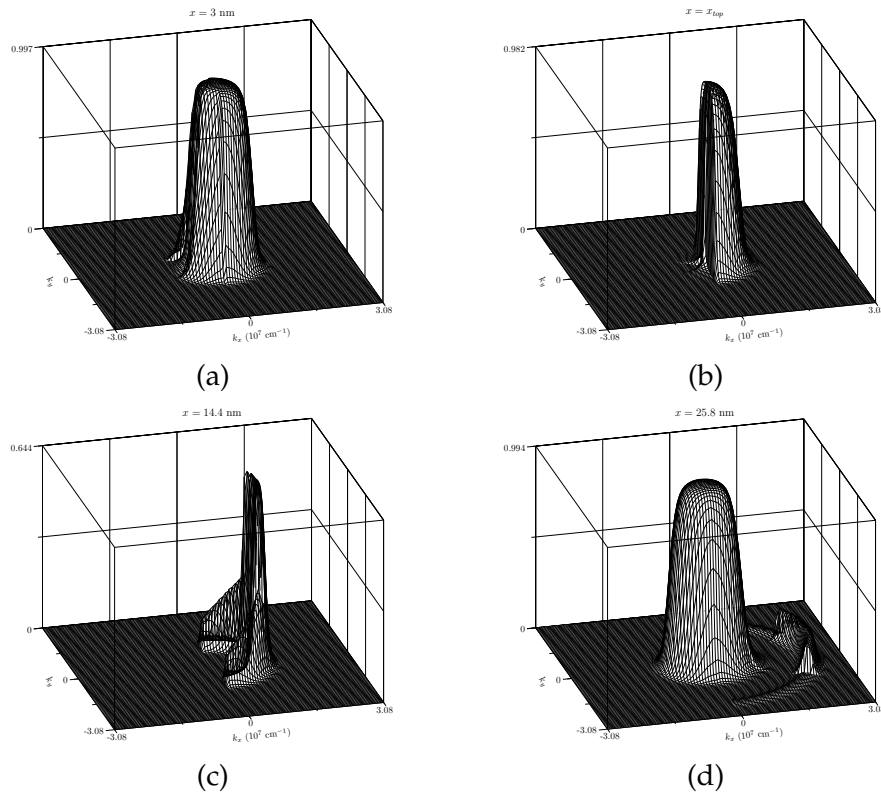


Figure 3: The pdf in the 1st subband  $f_0(x, k_x, k_y)$ . The S/D bias voltage  $V_{DS} = 0.5V$ . The gate voltage  $V_{G_{iS}} = V_{G_{dS}} = 0.3V$ .  $N_{scat} = 0$ .

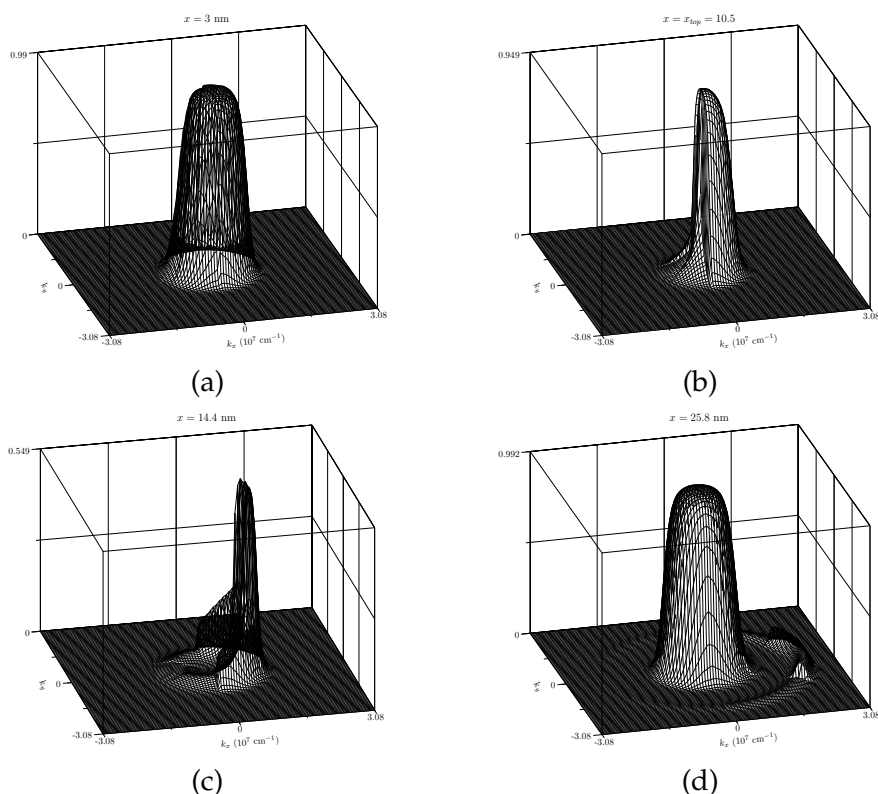


Figure 4: The pdf in the 1st subband  $f_0(x, k_x, k_y)$ . The S/D bias voltage  $V_{DS} = 0.5V$ . The gate voltage  $V_{G_{dS}} = V_{G_{dS}} = 0.3V$ .  $N_{\text{scat}} = 15$ .

$f_0(x, k_x, k_y)$  with  $N_{\text{scat}} = 15$ . The first subband reaches the peak value at the same location  $x_{\text{top}} = 10.5\text{nm}$  in both cases. Comparison of Fig. 3 and Fig. 4 shows more electrons are scattered to the negative  $k_x$  state. Besides that, we can observe the following facts from the two figures:

- Near the source/drain, electrons injected from the source/drain are reflected by the barrier, and build up a symmetric, thermal distribution. While a second peak is formed in the source extension due the accelerating electrons injected from the source. So the height of the pdf in the drain extension is a bit shorter than that in the drain.
- At the peak  $x_{\text{top}}$ , the pdf  $f_0$  changes abruptly along the  $k_x$ .
- In the channel, the electrons are accelerated to higher  $k_x$ .

Fig. 5, a plot of the electron density within the device under  $V_{DS} = 0.5V$  and  $N_{\text{scat}} = 15$ , shows the quantum confinement of electrons in the  $z$ -direction. The ballistic simulation and the simulation with scattering are compared in Fig. 6, which shows the integrated electron density versus position along the channel direction. It can be observed that more

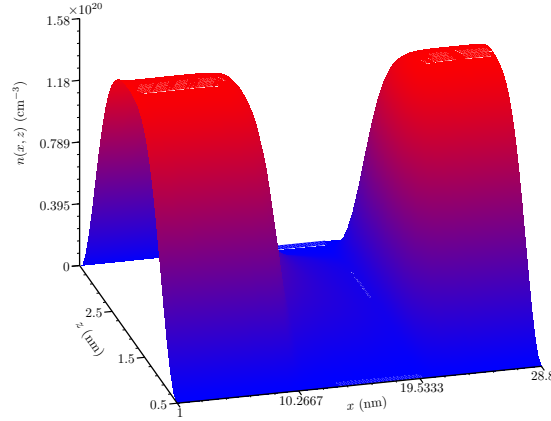


Figure 5: Total 3D electron density  $n(x,z)$ . The bias voltage  $V_{DS} = 0.5V$ .  $N_{scat} = 15$ .  $V_{G_{uS}} = V_{G_{dS}} = 0.3V$ . The electron density goes to zero at the top and bottom Oxide/Silicon interface  $x = 0.5nm$  and  $x = 3.5nm$  due to quantum confinement.

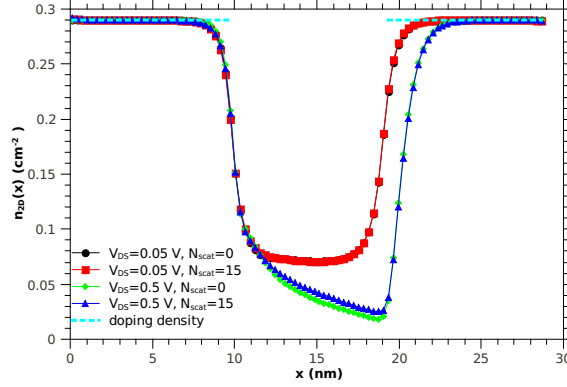


Figure 6: The 2D surface electron density  $n_{2D}(x)(cm^{-2})$  along the channel direction is plotted.  $V_{G_{uS}} = V_{G_{dS}} = 0.3V$ . The bias voltage  $V_{DS} = 0.05, 0.5V$ . Both the ballistic case ( $N_{scat} = 0$ ) and the scattering case ( $N_{scat} = 15$ ) are plotted.

electrons move into the channel due to scattering under high bias voltage. We can also see that the electron neutrality is obtained at the S/D region.

## 4.2 Scattering influence

In this subsection, we show the numerical results for asymmetric DG MSOFETs by changing the low gate voltage  $V_{G_{dS}}$  while fixing the upper gate voltage  $V_{G_{uS}} = 0.3V$ . The potential influences the current greatly and it is modulated by the gate bias voltage  $V_{G_{uS}}/V_{G_{dS}}$  and the S/D bias voltage  $V_{DS}$ . We plot a potential in Fig. 7 to show this modulation. Because of the natural boundary condition at the source/drain contact, the potential at the source/drain contact is not equal to the source/drain voltage.  $V = V_{G_{uS}}/V_{G_{dS}}$  at the

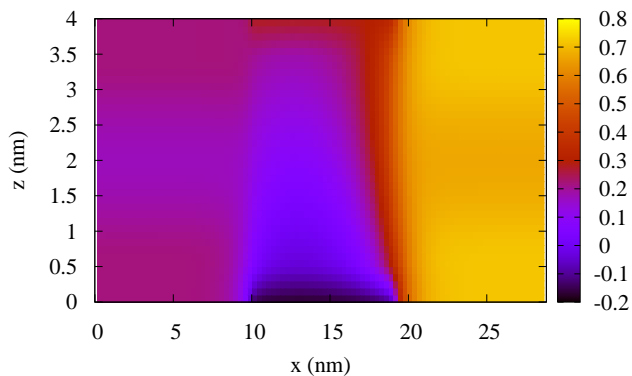


Figure 7: The potential of the stationary state of an asymmetric DG MOSFET. Two gate voltages are  $V_{G_{uS}}=0.3\text{V}$  and  $V_{G_{dS}}=-0.2\text{V}$ . The S/D bias voltage  $V_{DS}=0.5\text{V}$ .  $N_{\text{scat}}=15$ .

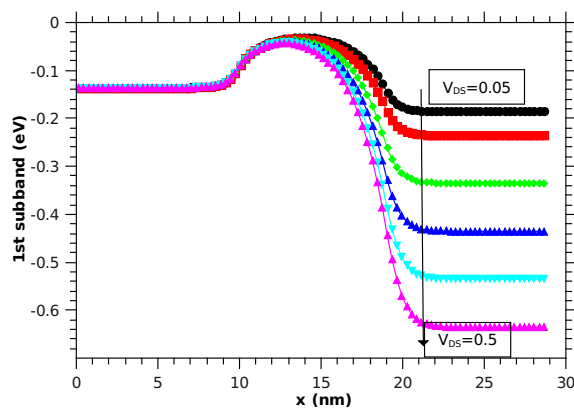


Figure 8: The first subband is modulated by  $V_{DS}$ .  $V_{DS}=0.05, 0.1, 0.2, 0.3, 0.4, 0.5\text{V}$ .  $V_{G_{uS}}=0.3\text{V}$  and  $V_{G_{dS}}=-0.2\text{V}$ .  $N_{\text{scat}}=15$ . The effect of  $V_{DS}$  on the 1st subband is clear.

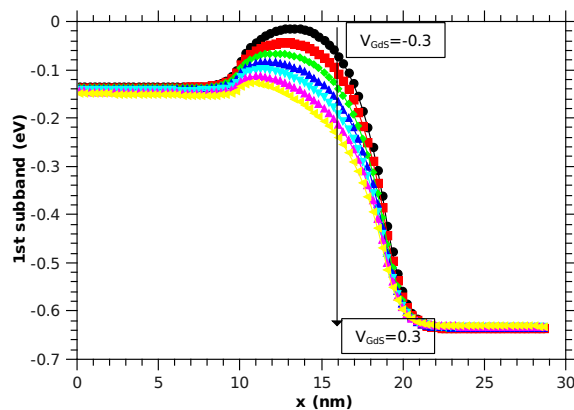


Figure 9: The first subband is modulated by  $V_{G_{dS}}$ .  $V_{G_{dS}}=-0.3, -0.2, \dots, 0.3\text{V}$ .  $V_{G_{uS}}=0.3\text{V}$  and  $V_{DS}=0.5\text{V}$ .  $N_{\text{scat}}=0$ . The height of the barrier in the first subband is adjusted by  $V_{G_{dS}}$ .

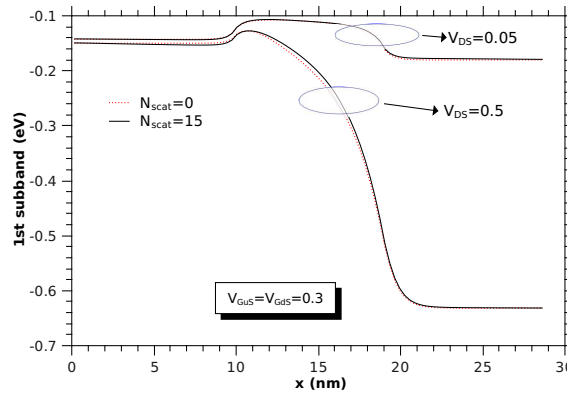


Figure 10: Comparison of the first subband with/without scattering. The scattering does make the shape of the first subband change greatly, and only makes the barrier raise less than 0.0006V higher.

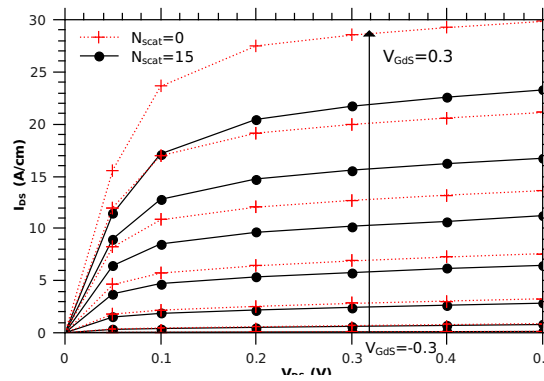


Figure 11: The current-voltage curves  $I_{DS} - V_{DS}$ . The lower gate voltages  $V_{G_dS} = -0.3, -0.2, \dots, 0.3V$ .  $V_{G_{dS}} = 0.3V$ .  $V_{D_S} = 0.05, 0.1, 0.2, \dots, 0.5V$ . The red dash dot lines are  $I_{D_S}$  under ballistic transport. The black lines are  $I_{D_S}$  under scattering. When  $V_{G_dS} = -0.3V$ , the current is smaller than 0.12A/cm.

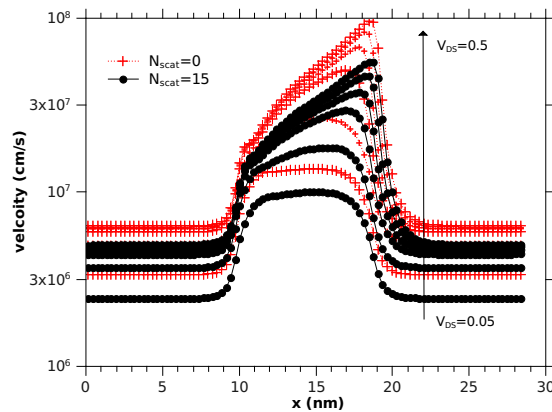


Figure 12: The drift velocity of electrons. We fix  $V_{G_{dS}} = V_{G_{dS}} = 0.3V$ . The red dotted lines are the velocity curves obtained ballistic transport, and the black solid line for scattering.  $V_{D_S} = 0.05, 0.1, 0.2, \dots, 0.5V$ . we can find scattering slows the electron velocity.

gate reflects the gate modulation of the potential clearly. Comparing the 1st subbands with/without scattering in Fig. 10, we find the scattering raises the subband a little higher in the channel which reflects the deformation of the barrier height due to scattering. We plot a series current-voltage curves  $I_{DS}-V_{DS}$  in Fig. 11. Comparison of the  $I_{DS}-V_{DS}$  curves in Fig. 11 shows the scattering lowers  $I_{DS}$  by about 10%–30%. From Fig. 11, we can also observe the  $I_{DS}-V_{DS}$  can be modulated by the lower gate bias voltage  $V_{GdS}$ . The subbands reflect the variation of the potential, so we plot the first subband in Fig. 8 to see the deformation of the potential due to the S/D bias voltage  $V_{DS}$ . We can observe the modulation of the potential due to  $V_{GdS}$  in Fig. 9, where the 1st subband for each  $V_{GdS}$  at a fixed  $V_{DS}$  is plotted. Finally, we plot the drift velocity of electrons in Fig. 12 where we can see scattering slows down electrons. Besides raising the barrier, Fig. 12 tells us that slowing the electron velocity is another aspect to explain why scattering lowers the S/D current  $I_{DS}$ .

## 5 Conclusions

We have developed a deterministic solver for the time-dependent Boltzmann-Schrödinger-Poisson system to simulate the nanoscale semiconductors. Complicated scattering mechanisms are considered in our deterministic solver. First, several types of scattering including intra-valley/inter-valley phonon-electron scattering are included. Second, the 2Dk scattering of the 2D electron gas due to the quantization in the confinement direction and the Pauli exclusion principle are used. We provide a second order solver for the BTE based on the PFC method, which is a flexible and powerful tool for simulating nanoscale devices, and allows variable time steps and positive and flux conservative approximation and convenient parallelization. As an example, a DG MOSFET with flared out source/drain contacts is simulated. Numerical results show that the scattering does influence the source-drain current unignorablely. And the deformation of subbands due to gate voltage and drain voltage is also investigated. This provides an alternative possibility to investigate the detail of the nanoscale MOSFETs. We are using the solver to investigate the different effect of intra-valley phonon-electron scattering and inter-valley phonon-electron scattering.

## Acknowledgments

The authors are grateful to Prof. Wei Cai for his helpful discussions. This work is supported by the NKBRP (Grants 2006CB302705, 2005CB321704) and the NSFC (Grants 10701005, 11011130029). T. Lu is sponsored by SRF for ROCS, SEM.

## References

- [1] N. Ben Abdallah, M. J. Cáceres, J. A. Carrillo, and F. Vecil, A deterministic solver for a hybrid quantum-classical transport model in nanoMOSFETs, *J. Comput. Phys.*, 228 (2009), 6553–

- 6571.
- [2] T. Ando, Alan B. Fowler, and F. Stern, Electronic properties of two-dimensional systems, *Rev. Mod. Phys.*, 54 (1982), 437–672.
  - [3] G. Bertrand, S. Deleonibus, B. Previtali, G. Guegan, X. Jehl, M. Sanquer, and F. Balestra, Towards the limits of conventional MOSFETs: case of sub 30nm NMOS devices, *Solid. State. Electron.*, 48 (2004), 505–509.
  - [4] F. Bouchut, F. Golse, and M. Pulvirenti, *Kinetic Equations and Asymptotic Theory*, GauthierVillars, Paris, 2000.
  - [5] J. A. Carrillo, I. M. Gamba, A. Majorana, and Chi-Wang Shu, A WENO-solver for the transients of Boltzmann-Poisson system for semiconductor devices: performance and comparisons with Monte Carlo methods, *J. Comput. Phys.*, 184 (2003), 498–525.
  - [6] S. Datta, Nanoscale device modeling: the Greens function method, *Superlattice. Microst.*, 28 (2000), 253–278.
  - [7] S. Datta, *Quantum Transport: Atom to Transistor*, Cambridge Univ. Press, Cambridge, U.K, 2005.
  - [8] F. Delaurens and F. J. Mustieles, A deterministic particle method for solving kinetic transport equations: the semiconductor Boltzmann equation case, *SIMA J. Appl. Math.*, 52 (1992), 973–998.
  - [9] V. Nam Do, P. Dollfus, and V. Lien Nguyen, Transport and noise in resonant tunneling diode using self-consistent green function calculation, *J. Appl. Phys.*, 100 (2006), 093705–093711.
  - [10] E. Fatemi and F. Odeh, Upwind finite difference solution of Boltzmann equation applied to electron transport in semiconductor devices, *J. Comput. Phys.*, 108 (1993), 209–217.
  - [11] E. Fijalkow, A numerical solution to the Vlasov equation, *Comput. Phys. Commun.*, 116 (1999), 319–328.
  - [12] F. Filbet and G. Russo, High order numerical methods for the space non-homogeneous Boltzmann equation, *J. Comput. Phys.*, 186 (2003), 457–480.
  - [13] F. Filbet and E. Sonnendrucker, Comparison of eulerian vlasov solvers, *Comput. Phys. Commun.*, 150 (2003), 247–266.
  - [14] F. Filbet, E. Sonnendrücker, and P. Bertrand, Conservative numerical schemes for the Vlasov equation, *J. Comput. Phys.*, 172 (2001), 166–187.
  - [15] R. Granzner, V. M. Polyakov, F. Schwierz, M. Kittler, and Doll T, On the suitability of DD and HD models for the simulation of nanometer double-gate MOSFETs, *Phys. E.*, 19 (2002), 33–38.
  - [16] M. A. Heroux, J. M. Willenbring, and R. Heaphy, *Trilinos developers guide*, Technical Report SAND2003-1898, Sandia National Laboratories, 2003.
  - [17] R. Lake, G. Klimeck, R. C. Bowen, and D. Jovanovic, Single and multiband modeling of quantum electron transport through layered semiconductor devices, *J. Appl. Phys.*, 81 (1997), 7845–7869.
  - [18] A. Majorana and R. M. Pizatella, A finite difference scheme solving the Boltzmann-Poisson system for semiconductor devices, *J. Comput. Phys.*, 174 (2001), 649–668.
  - [19] Z. B. Ren, *Nanoscale MOSFETs: Physics, Simulation, and Design*, PhD thesis, Purdue University, West Lafayette, IN, 2001.
  - [20] Z. Ren, R. Venugopal, S. Goasguen, S. Datta, and M. S. Lundstrom, nanoMOS 2.5: a two-dimensional simulator for quantum transport in double-gate MOSFETs, *IEEE Trans. Electron. Devices.*, 50 (2003), 1914–1924.
  - [21] J.-H. Rhew, Z. Ren, and M. S. Lundstrom, A numerical study of ballistic transport in a nanoscale MOSFET, *Solid. State. Electron.*, 46 (2002), 1899–1906.

- [22] S. Smirnov, Physical Modeling of Electron Transport in Strained Silicon and Silicon-Germanium, PhD thesis, Fakultät für Elektrotechnik und Informationstechnik, von, Wien, Österreich, 2003.
- [23] G. Strang, On the construction and comparison of difference schemes, *SIAM J. Numer. Anal.*, 5(1968), 506–517.
- [24] V. Sverdlov, E. Ungersboeck, H. Kosina, and S. Selberherr, Current transport models for nanoscale semiconductor devices, *Mat. Sc. Eng. R.*, 58 (2008), 228–270.
- [25] D. Ventura, A. Gnudi, G. Baccarani, and F. Odeh, Multidimensional spherical harmonics expansion of Boltzmann equation for transport in semiconductors, *Appl. Math. Lett.*, 5 (1992), 85–90.